Nano Research Energy

ISSN 2791-0091 CN 10-1944/O6
https://doi.org/10.26599/NRE.2026.9120269

Research Article

Fabrication of Multilayer Alternating Polymer-based Dielectric Composites with Superior Energy Storage Performance via Layer-by-layer Spraying Assembly

Renbo Wei[1], Shumin Bao[1], Yongxian Liu[1], Xiaofei Zhao[1], Yue Yu[1], Chunfang Lai[1], Lingling Wang[1](✉), Xiufu Hua[1,2](✉)

[1] Institute of Low-Carbon Technology Application, School of Chemical Engineering, Northwest University, Xi'an 710069, China

[2] Yangtze Delta Region Institute of Tsinghua University, Jiaxing 314006, China

Nano Research Energy, **Just Accepted Manuscript** • https://doi.org/10.26599/NRE.2026.9120269
https://www.sciopen.com/journal/2791-0091 on Aug. 18, 2026

Just Accepted

TABLE OF CONTENTS (TOC)

Fabrication of Multilayer Alternating Polymer-based Dielectric Composites with Superior Energy Storage Performance via Layer-by-layer Spraying Assembly

Renbo Wei[1], Shumin Bao[1], Yongxian Liu[1], Xiaofei Zhao[1], Yue Yu[1], Chunfang Lai[1], Lingling Wang[1]*, Xiufu Hua[1,2]*

[1]Institute of Low-Carbon Technology Application, School of Chemical Engineering, Northwest University, Xi'an 710069, China

[2]Yangtze Delta Region Institute of Tsinghua University, Jiaxing 314006, China

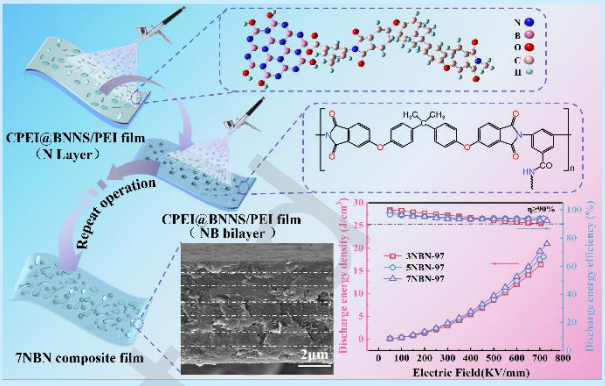

The alternating multilayer PEI-based composite film prepared by controllable layer-by-layer spraying assembly achieved a record energy density of 20.87 J·cm^{-3}.

Polymer-based dielectric composites are pivotal for advanced pulsed power and power electronics, yet synergistically enhancing dielectric constant and breakdown strength remains a formidable challenge. Herein, we report a controllable layer-by-layer spray assembly strategy to fabricate ordered multilayer polyetherimide (PEI)-based composites with alternating high-dielectric and high-insulation layers.

Renbo Wei, https://chin.nwu.edu.cn/info/1066/2094.htm

Xiufu Hua, https://chin.nwu.edu.cn/info/1068/3005.htm

Nano Research Energy

ISSN 2791-0091 (print); 2790-8119 (online)
https://doi.org/10.26599/NRE.2026.9120269

Research Article

Fabrication of Multilayer Alternating Polymer-based Dielectric Composites with Superior Energy Storage Performance via Layer-by-layer Spraying Assembly

Renbo Wei[1], Shumin Bao[1], Yongxian Liu[1], Xiaofei Zhao[1], Yue Yu[1], Chunfang Lai[1], Lingling Wang[1] (✉), and Xiufu Hua[1,2] (✉)

[1] *Institute of Low-Carbon Technology Application, School of Chemical Engineering, Northwest University, Xi'an 710069, China*
[2] *Yangtze Delta Region Institute of Tsinghua University, Jiaxing 314006, China*

Received: 9 June 2026 / **Revised:** 10 July 2026 / **Accepted:** 28 July 2026

ABSTRACT

Polymer-based dielectric composites are pivotal for advanced pulsed power and power electronics, yet synergistically enhancing dielectric constant and breakdown strength remains a formidable challenge. Herein, we report a controllable layer-by-layer spray assembly strategy to fabricate ordered multilayer polyetherimide (PEI)-based composites with alternating high-dielectric and high-insulation layers. Homologous carboxylated PEI (CPEI) was designed and covalently grafted onto boron nitride nanosheets (BNNS) and barium strontium titanate (BST) fillers, ensuring exceptional interfacial compatibility. This enabled the precise deposition of CPEI@BNNS/PEI and CPEI@BST/PEI layers, yielding 3-, 5-, and 7-layer films. The 7-layer film achieved a high dielectric constant of 7.43 at 1 kHz, a remarkable breakdown strength of 731.2 kV·mm^{-1}, and a record discharge energy density of 20.87 J·cm^{-3} — 4.91 times that of pure PEI — while maintaining >90% charge-discharge efficiency. Comprehensive characterization and simulations revealed that the alternating multilayer structure creates deep-level interface traps that effectively suppress space charge migration, homogenize the internal electric field, and block electrical tree propagation. This work provides a facile and scalable pathway for the design and fabrication of high-performance ultrathin dielectric films.

KEYWORDS

Layer-by-layer spray assembly; Polymer-based dielectrics; Energy storage performance; Multilayer structure.

1 Introduction

Dielectric capacitors, as core energy storage components for modern power electronic systems, have become irreplaceable in grid peak shaving, renewable energy conversion, and high-power pulsed power devices, primarily due to their inherent advantages of ultrafast charge/discharge rates, ultrahigh power density, and excellent long-term cycling stability compared to batteries and other electrochemical devices [1-4]. The relentless global push towards device miniaturization and high-density system integration has put forward an urgent requirement for a significant leap in the achievable energy density of dielectric materials [5]. Currently, the paramount fundamental challenge in this field lies in effectively transcending the inherent, long-standing trade-off between high dielectric constant and high breakdown strength [6-8].

While traditional polymeric dielectrics like polyetherimide (PEI) offer intrinsic advantages of high intrinsic breakdown strength and excellent mechanical flexibility [9-11], their naturally low dielectric constant (~3.2-3.4) severely limits the achievable energy storage density for practical applications [12, 13].

A widely adopted and prevalent strategy to address this challenge involves simultaneously incorporating high-dielectric-constant (high-*k*) ceramic nanofillers (e.g., barium strontium titanate (BST) [14], barium titanate (BT) [15]) into the polymer matrix to boost the overall polarization [16, 17], and wide-bandgap insulating nanomaterials (e.g., BNNS [18], Al2O3[19]) to enhance the composite's overall insulation [20, 21]. Nevertheless, the poor resultant interfacial incompatibility between inorganic fillers and the organic matrix often causes severe filler agglomeration, introducing numerous structural defects that easily trigger premature electrical breakdown under high electric fields [22]. Although targeted surface modification of fillers with organic polymer chains can effectively improve interfacial compatibility [23, 24], the intrinsic random dispersion of fillers in conventional blended composites still fundamentally fails to resolve the long-standing conflict between achieving simultaneous high polarization and high insulation [25, 26].

Address correspondence to Lingling Wang, wangll@nwu.edu.cn; Xiufu Hua, huaxf@nwu.edu.cn

TSINGHUA UNIVERSITY PRESS SciOpen

Inspired by the optimized hierarchical layered architectures found in natural high-performance biological structures, constructing artificial ordered multilayer films with alternating high-*k* dielectric layers and insulating functional layers has emerged as a particularly promising solution to break the aforementioned trade-off [27, 28]. This rational, bio-inspired hierarchical design allows each functional layer to exert its unique performance advantage optimally: the high-*k* layer maximizes the overall polarization of the film, while the insulating layer effectively homogenizes the internal electric field distribution and blocks unwanted charge injection from external electrodes [29, 30]. Although the concept of constructing layered structures with alternating functional layers has been explored, conventional fabrication methods (e.g., layer-by-layer spin-coating and solution casting) still struggle to achieve precise, scalable, and highly controllable layering for target ultrathin dielectric films. More importantly, the influence of the number of layers at a fixed total thickness—along with the associated mechanisms of electric field homogenization, space-charge suppression, and electrical treeing inhibition—remains insufficiently understood [31, 32].

To address these challenges, we propose a novel synergistic strategy that combines the concepts of homologous interface engineering and controllable spray-based layer-by-layer assembly. We rationally designed and synthesized carboxylated polyetherimide (CPEI) [33] as a compatibilizer to improve interfacial affinity for both BNNS insulators and BST high-k fillers, and further developed a precise spraying technique to facilely construct well-ordered multilayer films. This unique approach enabled us to systematically investigate the clear structure-property relationship of the composites, and ultimately developed a dielectric material with exceptional overall energy storage performance that outperforms most analogous materials.

2 Experimental Section

2.1 Materials

All chemicals were used as received. PEI was purchased from Adamas Company. Bisphenol A dianhydride (BPADA) and 3,5-diaminobenzoic acid (DBA) were obtained from Aladdin Company. More detailed information is provided in the Electronic Supplementary Material (ESM).

2.2 Synthesis of Carboxylated Polyetherimide (CPEI)

CPEI was synthesized via a one-pot polycondensation reaction using BPADA and DBA as the monomers (Figure S1, ESM) [33]. Full experimental details are described in the ESM.

2.3 Preparation of CPEI-grafted BNNS (CPEI@BNNS)

Hydroxylated BNNS (BNNS-OH) were prepared by liquid-phase ultrasonic exfoliation followed by alkali heat treatment [34]. Subsequently, CPEI was covalently grafted onto BNNS-OH via an esterification reaction. See ESM for detailed procedures.

2.4 Preparation of CPEI-grafted BST (CPEI@BST)

The surface of BST nanoparticles was modified using a two-step covalent grafting method [23]. Specific steps are outlined in the ESM.

2.5 Fabrication of Ordered Multilayer Composite Films via Controllable Spray Layer-by-Layer Assembly

A controllable layer-by-layer spray assembly strategy was developed to fabricate alternating multilayer composite films, and the detailed procedures are as follows. (1) Preparation of precursor solutions: quantified CPEI@BNNS and CPEI@BST were separately added into glass vials containing 10 mL DMAc and ultrasonicated for 2 h to obtain well-dispersed filler suspensions. Predetermined PEI were then added into the two suspensions respectively, and then magnetically stirred at 60 ℃ for 3 hours. After natural cooling, the mixtures were further stirred for 30 min to ensure complete dissolution of PEI and uniform blending with fillers. Two spraying precursors were successfully prepared, namely high-insulation CPEI@BNNS/PEI precursor and high-dielectric polarization CPEI@BST/PEI precursor. (2) Layer-by-layer spray assembly: clean glass substrates were preheated on a heating platform at 90 ℃. The two precursors were separately loaded into independent spray guns with a vertical distance of 15 cm between the spray gun and substrate, and sprayed at a uniform moving speed. After spraying each single layer, the substrate was kept static on the heating stage for 30 min to fully evaporate the solvent before spraying the next layer. Different functional layers were sequentially deposited via alternate spraying to acquire target multilayer films. (3) Post-treatment: after spraying, all samples were placed in a oven and dried at 150 ℃ for 1 h to fully eliminate residual solvents, thus obtaining ordered multilayer composite films with a total thickness of approximately 10 μm.

The layer containing CPEI@BNNS was defined as N layer, and the layer containing CPEI@BST was named as B layer. 3-layer (N-B-N), 5-layer (N-B-N-B-N), and 7-layer (N-B-N-B-N-B-N) films were fabricated, denoted as 3NBN-xy, 5NBN-xy, and 7NBN-xy, respectively, with x wt% of CPEI@BNNS and y wt% of CPEI@BST.

2.6 Characterization

Standard characterization techniques were employed. Fourier Transform Infrared (FTIR) spectra were measured with a BRUKER VERTEX70 TGA-IR spectrometer. Other detailed parameters are listed in the ESM.

3 Results and Discussion

In this work, well-ordered multilayer PEI-based composite dielectric films with alternating functional layer architectures were successfully fabricated via a controllable spray-based layer-by-layer assembly strategy. Fig. 1 systematically illustrates the overall fabrication and interfacial modification route adopted in this study. To optimize interfacial compatibility between inorganic fillers and the polymer matrix, carboxylated

polyetherimide (CPEI), which shares a homologous backbone structure with the PEI matrix, was rationally designed and synthesized. The full synthetic route of CPEI is provided in Figure S1 of the Electronic Supplementary Material (ESM). The 1H NMR spectrum, TGA profile, DSC curve, and molecular structure of CPEI are shown in Figures S2-S4 and Fig. 1(a), respectively. All characterization results collectively confirm the successful synthesis of CPEI.

Subsequently, two types of functional fillers were modified via covalent grafting separately. For high-dielectric barium strontium titanate (BST) nanoparticles, amination pretreatment was first performed using KH550. CPEI was then covalently grafted onto the aminated BST surface via an amidation reaction between the terminal carboxyl groups of CPEI and the surface amino groups of BST, yielding CPEI-grafted BST (CPEI@BST) (Fig. 1(b)). For insulating boron nitride, hydroxylated boron nitride nanosheets (BNNS-OH) were first prepared via liquid-phase ultrasonic exfoliation combined with an alkali hydrothermal treatment. CPEI was further covalently grafted onto BNNS-OH via an esterification reaction to obtain interfacially modified CPEI-grafted BNNS (CPEI@BNNS), as depicted in Fig. 1(c). This homologous polymer modification strategy effectively improves the interfacial interaction of the fillers with the PEI matrix, and avoids the performance degradation caused by uncontrolled filler aggregation.

On this basis, a controllable layer-by-layer spraying method (Fig. 1(d)) was employed to alternately deposit CPEI@BNNS/PEI high-insulation charge-blocking layers and CPEI@BST/PEI high-dielectric polarization layers. By designing the outermost layers as insulating CPEI@BNNS/PEI, three-layer structured composite films (3NBN) with different filler loadings were fabricated. After determining the optimal filler content, five-layer (5NBN) and seven-layer (7NBN) multilayer films were further prepared. Finally, the dielectric properties, energy storage performance, mechanical properties, and thermal stability of the multilayer films with different layer numbers were systematically compared. Combined with structural characterization and theoretical simulation, the regulation mechanism of the multilayer architecture on the comprehensive performance of the composite dielectrics was clarified.

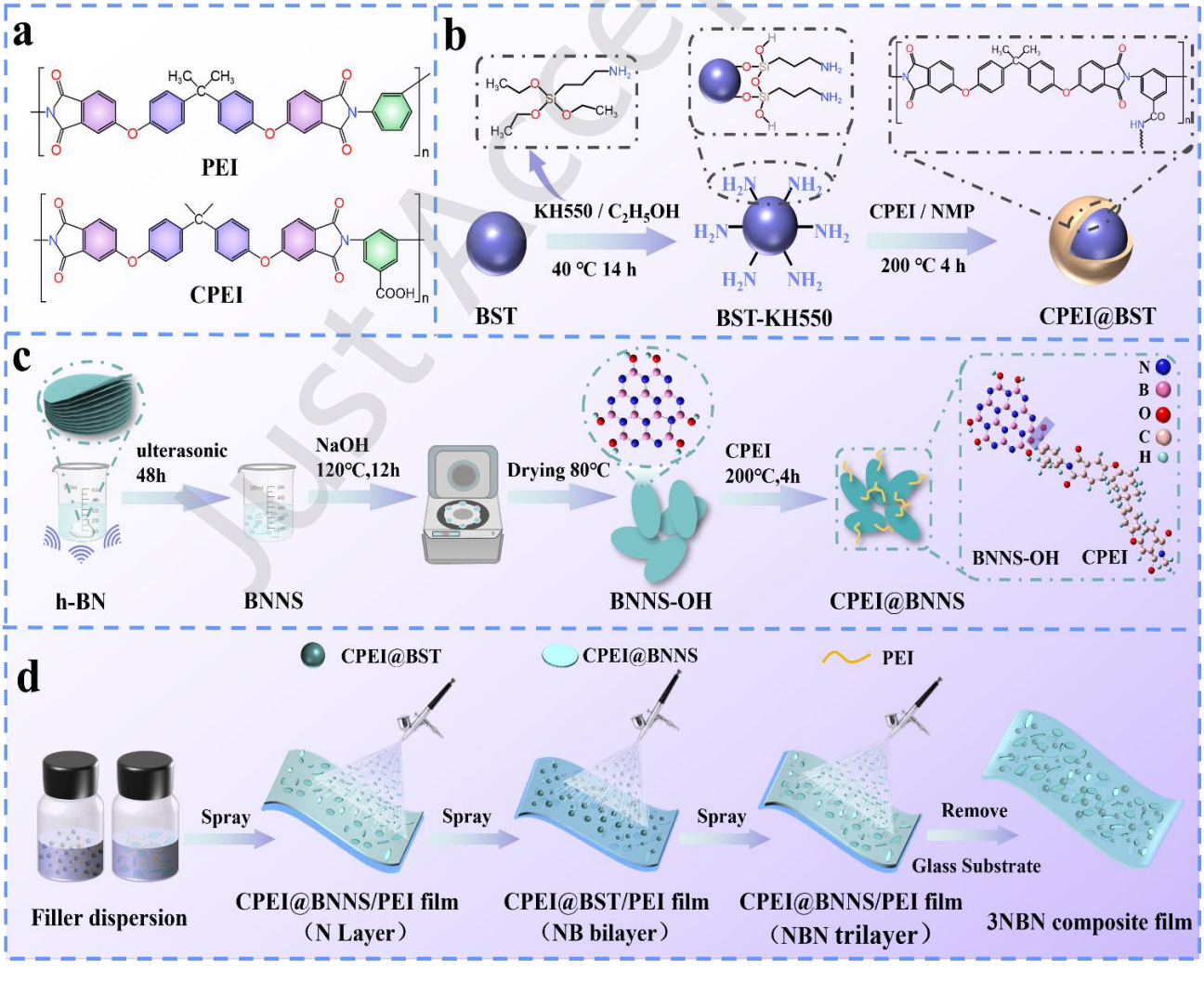

Figure 1 (a) Structure of PEI and CPEI. (b) Preparation diagram for CPEI@BST. (c) Preparation process of CPEI@BNNS. (d) Preparation

process of 3NBN composite film.

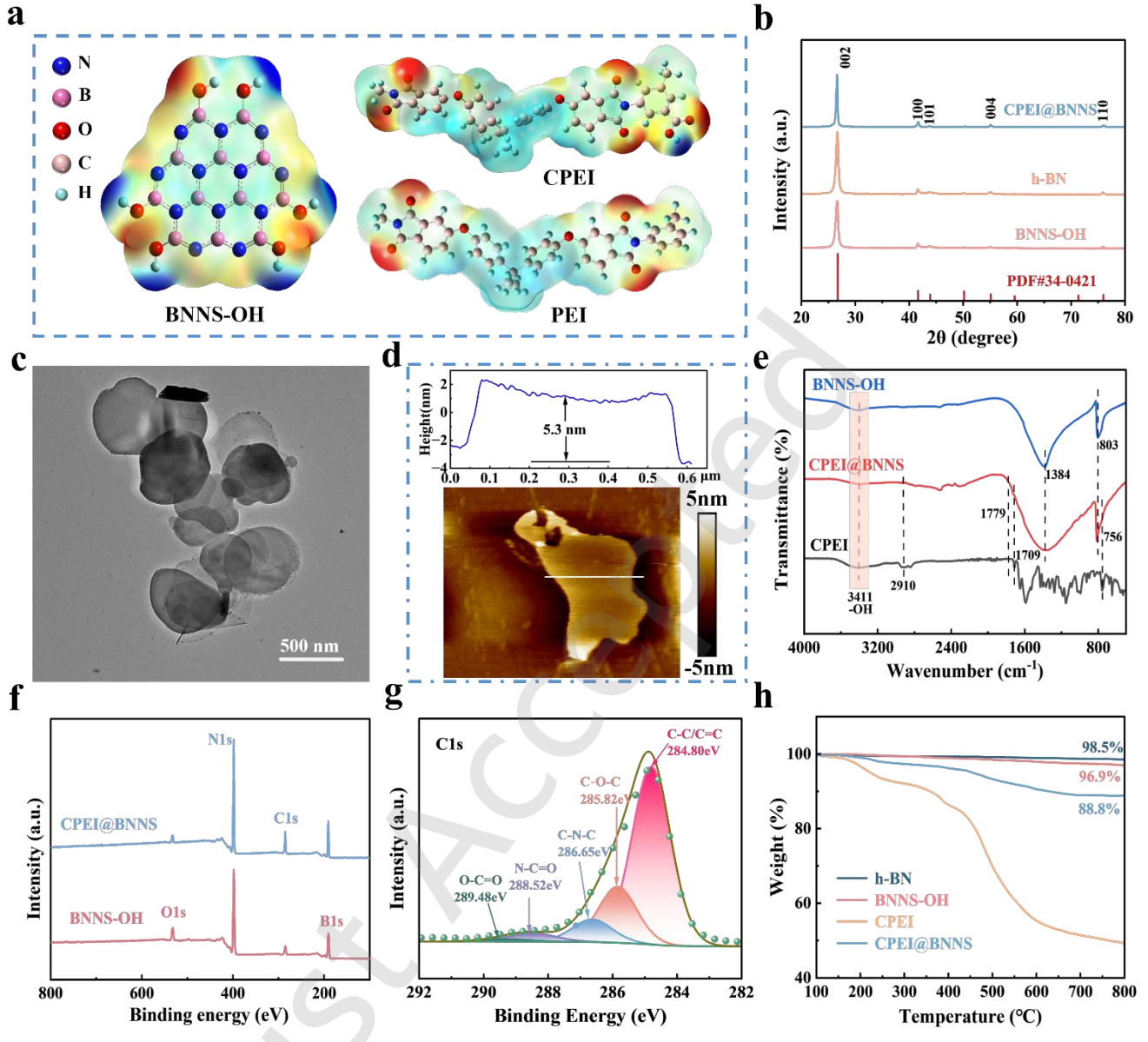

Figure 2 (a) Electrostatic potential energy distribution diagram of BNNS-OH, CPEI and PEI. (b) XRD patterns of h-BN, BNNS-OH, and CPEI@BNNS. (c) TEM image and (d) AFM image of CPEI@BNNS. (e) FTIR spectra of BNNS-OH, CPEI, and CPEI@BNNS. (f) XPS spectra of BNNS-OH and CPEI@BNNS. (g) C1s spectrum of CPEI@BNNS. (h) TGA curves of h-BN, BNNS-OH, CPEI and CPEI@BNNS.

Molecular electrostatic potential calculations (Fig. 2(a)) reveal distinct positive electrostatic potential regions on the carboxyl groups of CPEI and negative regions on the hydroxyl groups of BNNS-OH, respectively. This intrinsic electrostatic complementarity provides the thermodynamic driving force for the esterification reaction and subsequent covalent grafting, validating the rationality of our interfacial design [34]. XRD patterns (Fig. 2(b)) show that the positions of the characteristic diffraction peaks of pristine h-BN, BNNS-OH, and CPEI@BNNS are nearly identical, confirming that the hexagonal crystal structure of boron nitride is well retained during exfoliation and modification. Compared with *h*-BN, the intensities of the (002), (100), and (110) diffraction peaks of BNNS-OH are significantly reduced, which is a typical characteristic of decreased layer number, reduced lateral size, and increased structural disorder after liquid-phase exfoliation [35]. Notably, the (002) peak of CPEI@BNNS shifts to a lower 2θ angle relative to that of BNNS-OH, indicating an expansion of interlayer spacing and verifying the successful functional modification.

Furthermore, FTIR was used to characterize the chemical structure of all samples, with the results presented in Fig. 2(c). In the spectra of h-BN and BNNS-OH, the characteristic stretching vibration peaks at 1384 and 803 cm^{-1} are assigned to B-N in-plane stretching and B-N-B out-of-plane bending, respectively. A distinct stretching vibration peak of hydroxyl groups appears at 3411 cm^{-1} in the spectrum of BNNS-OH, confirming that hydroxyl groups are successfully introduced onto the

surface of exfoliated boron nitride nanosheets [34]. For the synthesized CPEI, the absorption peak at 1779 cm^{-1} is attributed to the symmetric stretch of C=O in the backbone imide groups, while the characteristic band at 1709 cm^{-1} corresponds to the symmetric stretch of C=O in the side-chain carboxyl groups, which confirms the successful synthesis of carboxylated polyetherimide [36]. The FTIR spectrum of CPEI@BNNS retains all characteristic peaks of both CPEI and BNNS without obvious peak shifts, confirming successful grafting with preserved chemical structures of both components.

XPS was further utilized to analyze the surface chemical states of CPEI@BNNS, with the corresponding results shown in Figs. 2(f), 2(g). By comparing the full survey spectra of pristine h-BN and BNNS-OH (Fig. 2(f) and Figure S5), it is evident that the signal intensity of O1s in hydroxylated BNNS-OH is remarkably enhanced, verifying the successful introduction of surface hydroxyl groups [37]. Peak fitting of the high-resolution C1s spectrum of CPEI@BNNS (Fig. 2(g)) yields five characteristic peaks, which are assigned to C-C/C=C (284.8 eV), C-O-C (285.82 eV), C-N-C (286.65 eV), N-C=O (288.52 eV), and O-C=O (289.48 eV), respectively. The appearance of the C-O-C and O-C=O peaks directly confirms that the esterification reaction occurs between the surface hydroxyl groups in BNNS-OH and the side-chain carboxyl groups at CPEI, forming stable covalent bonds. This conclusion is further supported by the high-resolution N1s and B1s spectra: an obvious characteristic peak assigned to N-C=O emerges at 400.02 eV in the N 1s spectrum of CPEI@BNNS, and the B-O characteristic peak in the B1s spectrum shifts to 191.46 eV (Figure S6). These results collectively verify the successful implementation of the covalent grafting reaction [15].

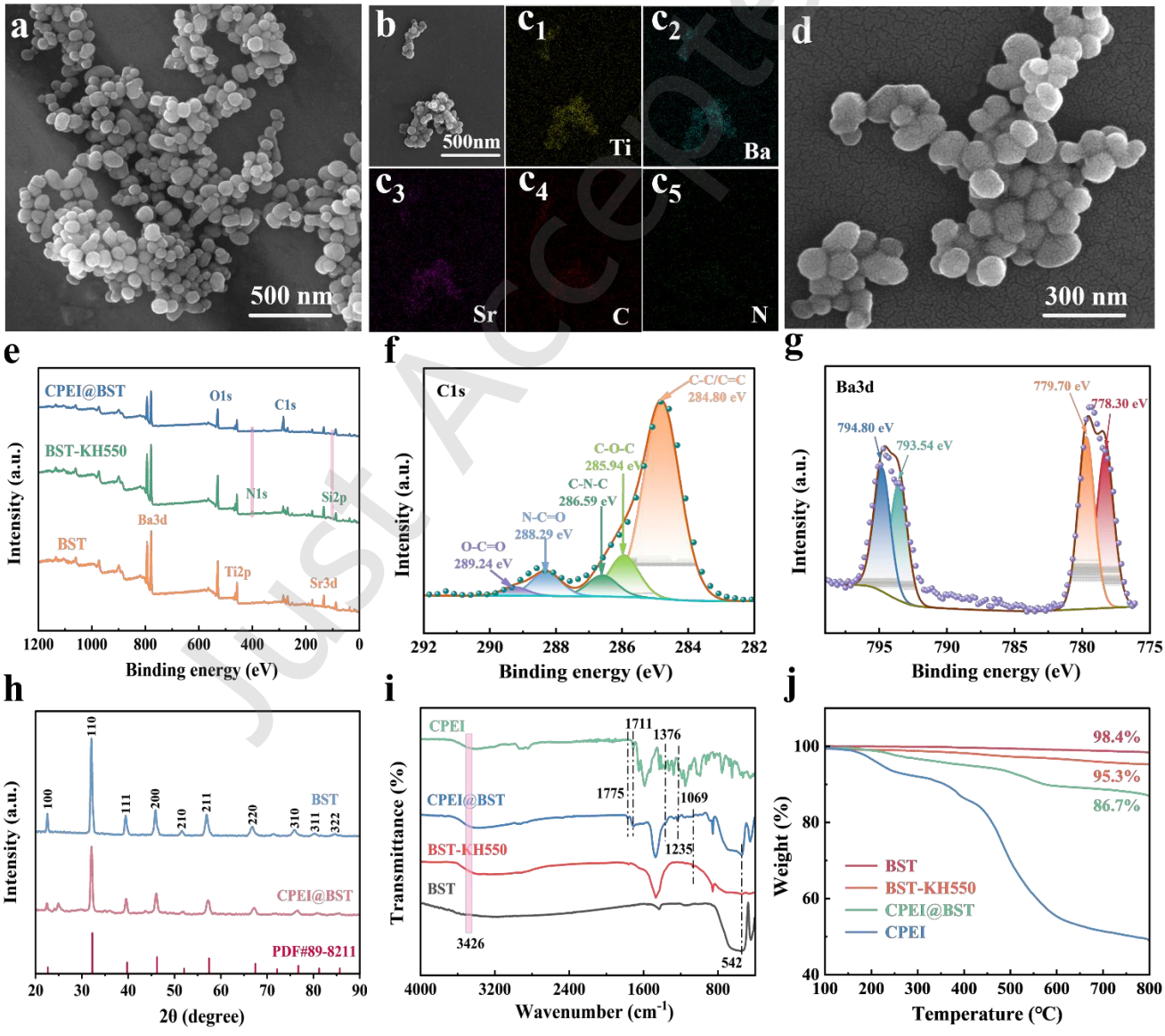

Figure 3 SEM images of (a) BST and (d) CPEI@BST. (b, c) SEM and corresponding mapping images of CPEI@BST. (e) XPS spectra of BST, BST-KH550, and CPEI@BST. (f) C1s, (g) Ba3d spectrum of CPEI@BST. (h) XRD patterns of BST and CPEI@BST. (i) FTIR spectra of BST, BST-KH550, CPEI, and CPEI@BST. (j) TGA curves of BST, BST-KH550, CPEI and CPEI@BST.

TEM and AFM characterizations (Figs. 2(c),2(d)) reveal that the modified CPEI@BNNS still maintains an intact lamellar structure with an average thickness of approximately 5.3 nm and a uniform lateral size distribution [35]. Compared with the morphological results of h-BN (Figures S7, S8), it can be observed that boron nitride nanosheets show no obvious agglomeration after liquid-phase exfoliation and CPEI grafting modification, and possess excellent dispersibility in organic solvents (Figure S9), which provides a favorable foundation for subsequent film fabrication. The UV-Vis absorption spectrum of BNNS (Figure S10(a)) presents an absorption peak at approximately 210 nm, which is consistent with previous literature reports [34]. Figure S10(b) shows the band gap value (Eg = 5.65 eV) calculated via the Tauc plot method (Note S1, ESM), confirming the successful preparation of BNNS with the desired wide-bandgap characteristics.

TGA curves (Fig. 2(h)) further quantitatively verify the grafting ratio of CPEI. Pristine h-BN only exhibits a mass loss of approximately 1.5 wt% from room temperature to 800 ℃, demonstrating its outstanding intrinsic thermal stability. The total mass loss of CPEI@BNNS is about 9.7 wt%. After excluding the inherent mass loss of BNNS-OH and combining with the thermal decomposition curve of pure CPEI, the grafting ratio of CPEI on the BNNS surface is calculated to be around 8.2 wt%. Moreover, the characteristic thermal decomposition temperature (~530 ℃) [38] of CPEI@BNNS is consistent with that of neat CPEI, which further evidences the successful covalent grafting.

Next, SEM was used to characterize the micromorphology and elemental distribution of pristine BST and CPEI@BST, with the corresponding results presented in Figs. 3(a)-3(d) and Figure S11. The SEM elemental mapping results distinctly exhibit the uniform distribution of carbon elements on the surface of the modified BST particles, preliminarily confirming the successful grafting of CPEI onto BST surfaces. To further clarify the chemical bonding state and elemental composition on the BST surface, XPS measurements were carried out, and the findings are displayed in Fig. 3(e). Compared with pristine BST, obvious new characteristic peaks of Si2p and N1s appear in the full XPS survey spectra of samples pre-modified with KH550. After subsequent CPEI grafting, the signal intensities of C1s and N1s in the full spectrum of CPEI@BST are further markedly enhanced, while the intensities of other elemental characteristic peaks decrease relatively, which is in good accordance with the variation rule of surface elements induced by organic layer grafting [39]. Peak fitting of C1s in CPEI@BST (Fig. 3(f)) yields five characteristic peaks at 284.80, 285.94, 286.59, 288.29, and 289.24 eV, respectively. Among them, the C-O-C peak at 285.94 eV and the N-C=O peak at 288.29 eV serve as direct evidence for the successful grafting of CPEI molecular chains. For Ba and Sr elements, their high-resolution 3d spectra exhibit typical spin-orbit splitting doublets (Fig. 3(g) and Figure S12(b)), which is consistent with their standard electronic structural characteristics. The Ti2p spectrum displays two characteristic peaks at 457.7 and 463.4 eV, which are assigned to $Ti2p_{3/2}$ and $Ti2p_{1/2}$, respectively (Figure S12(a)). This result confirms that titanium exists in the stable Ti^{4+} oxidation state within BST [40]. The above XPS results clearly elucidate the surface chemical structure of CPEI@BST, further verifying the success of the targeted modification [41].

Fig. 3(h) illustrates the XRD patterns of pristine BST and CPEI@BST. All characteristic diffraction peaks of BST are well consistent with those of standard cubic perovskite-structured barium strontium titanate (PDF#89-8211), which confirms that the as-synthesized BST possesses a high-purity perovskite crystal structure [42]. For CPEI@BST, the positions of characteristic diffraction peaks are entirely identical to those of pristine BST with only a slight decline in peak intensity, demonstrating that the encapsulation modification by CPEI organic layers does not damage the intrinsic crystal structure of BST. FTIR served to characterize the chemical bond structures for the samples within the wavenumber range of 4000-400 cm^{-1}, and the results are displayed in Fig. 3(i). The characteristic absorption peak of BST at 542 cm^{-1} is attributed to the stretching mode of Ti-O bonds [43]. As for BST-KH550, the newly emerged peak at 1069 cm^{-1} corresponds to the Si-O-C bonds formed between the BST surface and KH550, verifying the successful grafting of the silane coupling agent. Compared with the spectra of pure BST and CPEI, no obvious shift is observed for all characteristic peaks of CPEI@BST, indicating the successful grafting of CPEI and the well-preserved intrinsic chemical structures of each component.

TGA curves (Fig. 3(j)) further quantitatively confirm the modification process and grafting content. Pristine BST exhibits negligible mass loss within the range of 100-800 ℃, revealing its superior intrinsic thermal stability. After CPEI grafting, the residual mass of CPEI@BST decreases to 86.7 wt% at 800 ℃. By excluding the mass contribution of KH550, the successful immobilization of CPEI on the BST surface is confirmed. In summary, the characterization results from SEM, XPS, XRD, FTIR, and TGA are mutually consistent, collectively verifying the successful fabrication of core-shell structured CPEI@BST nanofillers.

To demonstrate the superiority of the homologous CPEI modification strategy, we prepared control samples using

KH550-modified BNNS and BST fillers under identical conditions (9 wt% BNNS, 7 wt% BST, and three-layer architecture). As shown in Figures S32-S34, the CPEI-modified composites exhibit significantly better filler dispersion and interfacial adhesion, with no obvious microvoids or agglomerates. Leakage current measurements reveal that the CPEI-modified composites show a current density of 7.6×10^{-8} A·cm^{-2} at 100 MV·m^{-1}, which is markedly lower than that of the KH550-modified samples (1.9×10^{-7} A·cm^{-2}). Correspondingly, the breakdown strength and discharge energy density of the CPEI-modified composites (705.3 kV·mm^{-1} and 16.38 J·cm^{-3}) are substantially higher than those of the KH550-modified counterparts (668.7 kV·mm^{-1} and 13.43 J·cm^{-3}). These results collectively confirm that the homologous CPEI grafting strategy is superior to conventional coupling-agent modification in enhancing interfacial compatibility and overall dielectric performance.

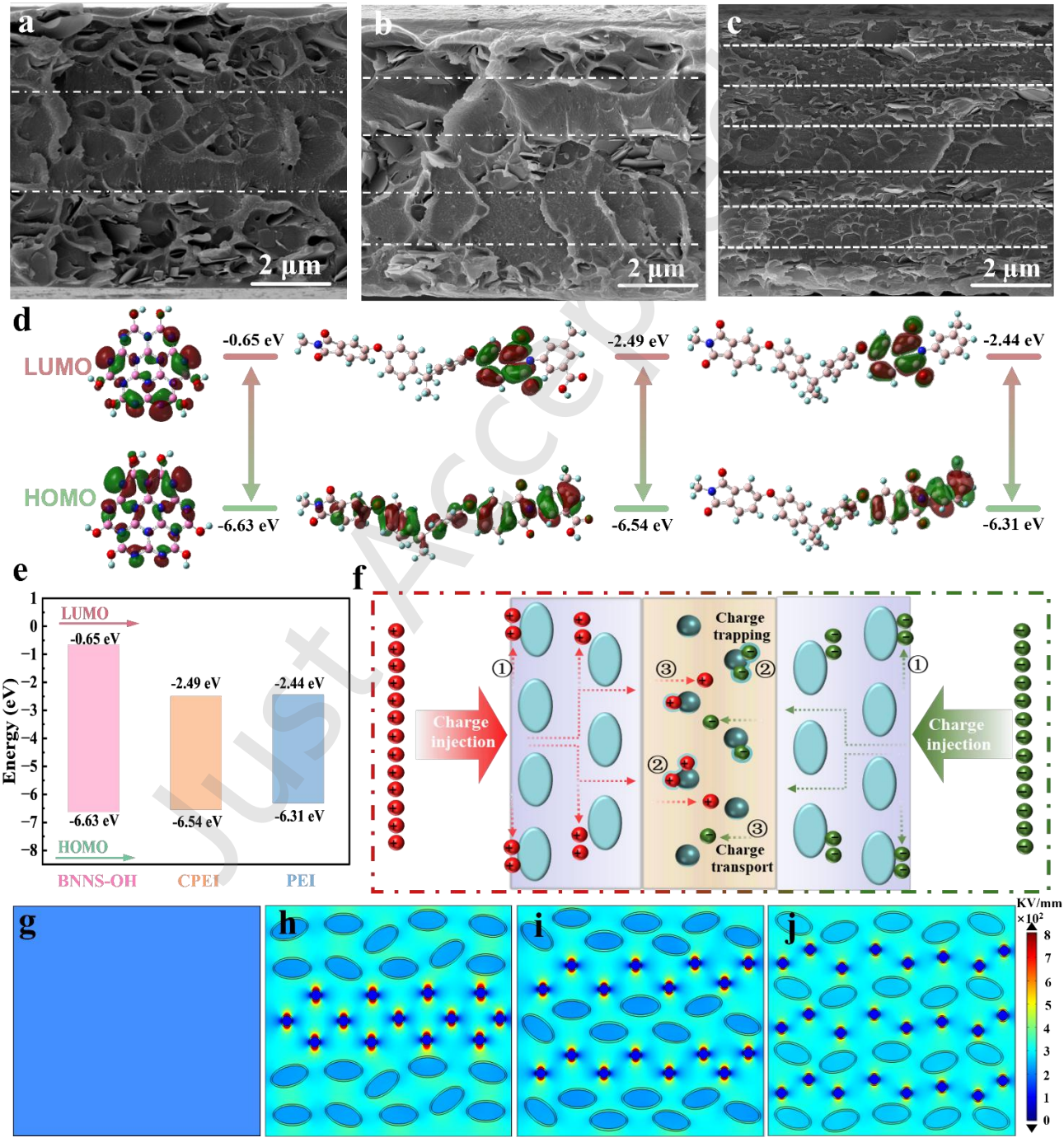

Figure 4 SEM images of (a) 3NBN-97, (b) 5NBN-97, (c) 7NBN-97. (d, e) The energy level distribution of BNNS-OH, CPEI and PEI. (f) By introducing the BNNS and BST layer mechanisms to suppress injected charge. (g-j) Electric field distribution of pure PEI, 3NBN-97, 5NBN-97 and 7NBN-97 films at an electric field of 400 kV·mm^{-1}.

After the successful preparation of CPEI@BNNS and CPEI@BST functional fillers, these two fillers were hierarchically incorporated into the PEI matrix via the controllable spray-based layer-by-layer assembly strategy, and ordered multilayer PEI-based composite films with alternating functional layer architectures were accordingly fabricated. Figs. 4(a)-4(c) and Figure S13 present the cross-sectional SEM micrographs and respective distribution models of 3NBN-97, 5NBN-97, and 7NBN-97 composite films, which contain 9 wt% CPEI@BNNS and 7 wt% CPEI@BST. Continuous and well-defined alternating layered structures can be clearly observed in all samples. Meanwhile, the total thickness of all samples with different layer numbers is precisely regulated to be identical, which confirms that this controllable spray-based layer-by-layer assembly strategy enables the accurate construction of multilayer composite films with highly ordered architectures.

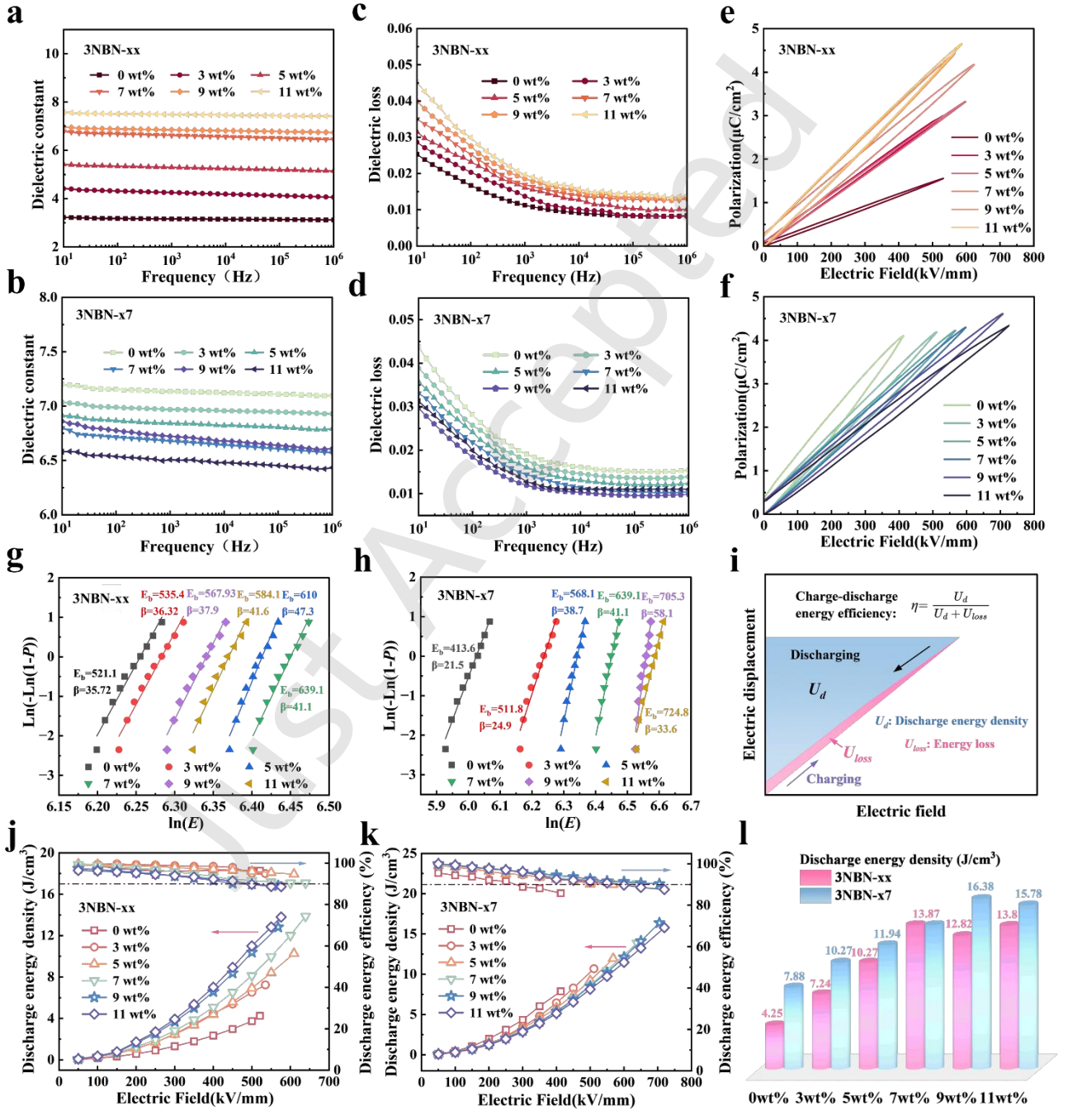

Figure 5 Dielectric constants of (a) 3NBN-xx and (b) 3NBN-x7. Dielectric loss of (c) 3NBN-xx and (d) 3NBN-x7. P-E loops of (e) 3NBN-xx and (f) 3NBN-x7. Weibull distribution plots of breakdown strength of (g) 3NBN-xx and (h) 3NBN-x7. (i) The schematic of the P-E loop for dielectrics. U_d and η of (j) 3NBN-xx and (k) 3NBN-x7. (l) Energy storage comparison.

Nano Research Energy
ISSN 2791-0091 (print); 2790-8119 (online)
https://doi.org/10.26599/NRE.2026.9120269

The thermal and mechanical properties of the as-prepared NBN multilayer composite films were systematically studied. The DSC results are displayed in Figures S14, S15. The glass transition temperature (T_g) of all NBN multilayer composite films is higher than 210 ℃, demonstrating the outstanding high-temperature resistance of this composite system [38]. For the 3NBN system, T_g gradually increases from 216.9 to 225.1 ℃ as the total loading of CPEI@BNNS and CPEI@BST increases. When the total filler content remains constant, T_g of the multilayer system further rises from 223.9 to 226.4 ℃ as the number of alternating layers increases from 3 to 7. Such improvement is attributed to the fact that the well-ordered alternating multilayer architecture optimizes filler dispersion in the matrix, and the enhanced interfacial interaction restricts the segmental mobility of PEI molecular chains, thereby ultimately elevating the T_g of the composite system. All multilayer composite films exhibit less than 10% mass loss below 500 ℃, exhibits good thermal stability with potential for high-temperature applications (Figures S16, S17). The char residue at 800 ℃ increases with higher CPEI@BNNS and CPEI@BST loadings, which is consistent with the typical thermal degradation behavior of inorganic filler-reinforced polymer systems.

Subsequently, the dielectric characteristics of the NBN multilayer composite films were systematically investigated. Figs. 5(a),5(b) illustrate the frequency dependent permittivity of 3NBN composite films with different filler loadings. All samples exhibit excellent frequency stability of dielectric constant over the measured frequency range. At 1 kHz (Figure S19), the dielectric constant of 3NBN-xx increases from 3.16 (pristine PEI) to 7.48 with increased loading of CPEI@BNNS and CPEI@BST. When the CPEI@BST content is fixed, the dielectric constant of the 3NBN-x7 system decreases from 7.12 to 6.47 as the CPEI@BNNS loading increases, which is attributed to the intrinsic difference in dielectric constant between the two fillers: BST has a high intrinsic dielectric constant, whereas BNNS exhibits a low intrinsic dielectric constant (~5), much lower than that of BST. Therefore, increasing CPEI@BNNS content reduces the overall dielectric constant of the composite. Figs. 5(c), 5(d) present the frequency-dependent dielectric loss of the 3NBN systems. All samples maintain dielectric loss below 0.05 over the entire tested frequency range, which benefits from the CPEI surface modification of both BST and BNNS. The modified fillers show greatly improved compatibility and dispersibility with the PEI matrix, which facilitates interfacial polarization, lowers the relaxation energy barrier of polarized charges, and effectively suppresses leakage current loss caused by interfacial defects. As a result, the synergistic optimization of increased dielectric constant and reduced dielectric loss is achieved.

Breakdown strength (E_b) is another critical parameter governing the energy storage density of dielectric materials. In this work, a Weibull distribution with two-parameter was used to fit the E_b data (Figs. 5(g),5(h)) [44]. All tested samples exhibit Weibull values of β>10, confirming high data reliability and good statistical confidence. For the 3NBN-xx series, with increasing total filler loading, the E_b first increases and then decreases, peaking at 639.1 kV·mm^{-1} at 7 wt% total loading. The excellent intrinsic insulation of boron nitride nanosheets (BNNS) enables effective scattering and trapping of mobile space charges, which reduces the overall space charge density and leakage current density, consequently enhancing the breakdown strength of the composite. However, an excessive loading of high-dielectric BST nanoparticles introduces a large number of interfacial defects, disrupts the continuity of the insulating polymer matrix, and causes severe local electric field distortion, which ultimately degrades the breakdown performance. Similarly, when the CPEI@BST content is fixed and the CPEI@BNNS loading is varied, the E_b of the 3NBN-x7 system also follows a trend of an initial rise followed by a fall. A suitable content of CPEI@BNNS provides effective insulating barriers to block charge propagation, while excessive loading causes filler agglomeration, structural inhomogeneity, and local electric field concentration, leading to performance degradation. After systematic component optimization, the 3NBN-97 composite achieves a high E_b of 705.3 kV·mm^{-1}, which lays a solid foundation for achieving high energy storage density. Leakage current density measurements (Figures S20, S21) further validate this mechanism. All xNBN films demonstrate excellent electrical insulation, and notably, the best among the investigated layer numbers 7NBN-97 sample exhibits the strongest leakage current suppression capability. At an applied electric field of 100 MV·m^{-1}, its leakage current density is as low as 1.6×10^{-8} A·cm^{-2}, which is one order of magnitude lower than that of neat PEI (4.2×10^{-7} A·cm^{-2}). This result directly confirms, from the perspective of charge transport behavior, that the ordered multilayer structure effectively enhances the Eb of the composite dielectric.

To reveal the molecular-level regulation mechanism of interfacial modification on dielectric properties, density functional theory (DFT) simulations [45] were conducted to calculate the electronic energy level structures of hydroxylated boron nitride nanosheets (BNNS-OH), neat PEI, and CPEI (Note S2 in the ESM), with the results presented in Figs. 4d, 4e. The calculated band gaps of PEI and CPEI are 3.87 and 4.05 eV, respectively, both of which are significantly lower than the band gap of 5.98 eV for BNNS-OH. This indicates that conduction band electrons in CPEI are more easily excited and can spontaneously migrate toward the conduction band of BNNS-OH. The wider band gap of CPEI compared to PEI originates from the introduction of side-chain carboxyl groups, which disrupt the conjugated architecture of the polymer backbone, reduce electron delocalization, and consequently broaden the band gap [46]. The gradient

energy level structure formed by the narrow-band-gap CPEI modification layer and the wide-band-gap BNNS guides the directional migration of charge carriers, facilitates deep trap capture of carriers by BNNS, and ultimately suppresses leakage current. Based on the DFT calculations, we propose a charge injection suppression mechanism for the NBN multilayer structure (Fig. 4(f)). In the three-layer composite films consisting of outer CPEI@BNNS/PEI insulating layers and an inner CPEI@BST/PEI functional layer, multiple synergistic effects work together to inhibit charge injection: (1) the outer insulating layers exploit the wide band gap of BNNS[14] to increase the Schottky barrier height at the electrode-dielectric interface, blocking most carrier injection at the source; (2) interfacial traps between BNNS and the PEI further capture and localize the small number of injected charges, hindering their long-range inward migration; (3) the inner CPEI@BST/PEI layer acts as the energy-storage functional layer, providing high polarization via the high dielectric constant of BST; and (4) the abundant internal filler-matrix interfaces introduce additional trap scattering and trapping effects, which further slow the long-range migration of charge carriers. This layered synergistic structure, which combines a high-barrier outer layer, a high-polarization inner layer, and multilayer interfacial trap regulation, suppresses leakage current through barrier elevation, interfacial charge trapping, and tortuous migration pathways, thereby enhancing the overall dielectric performance of the composite.

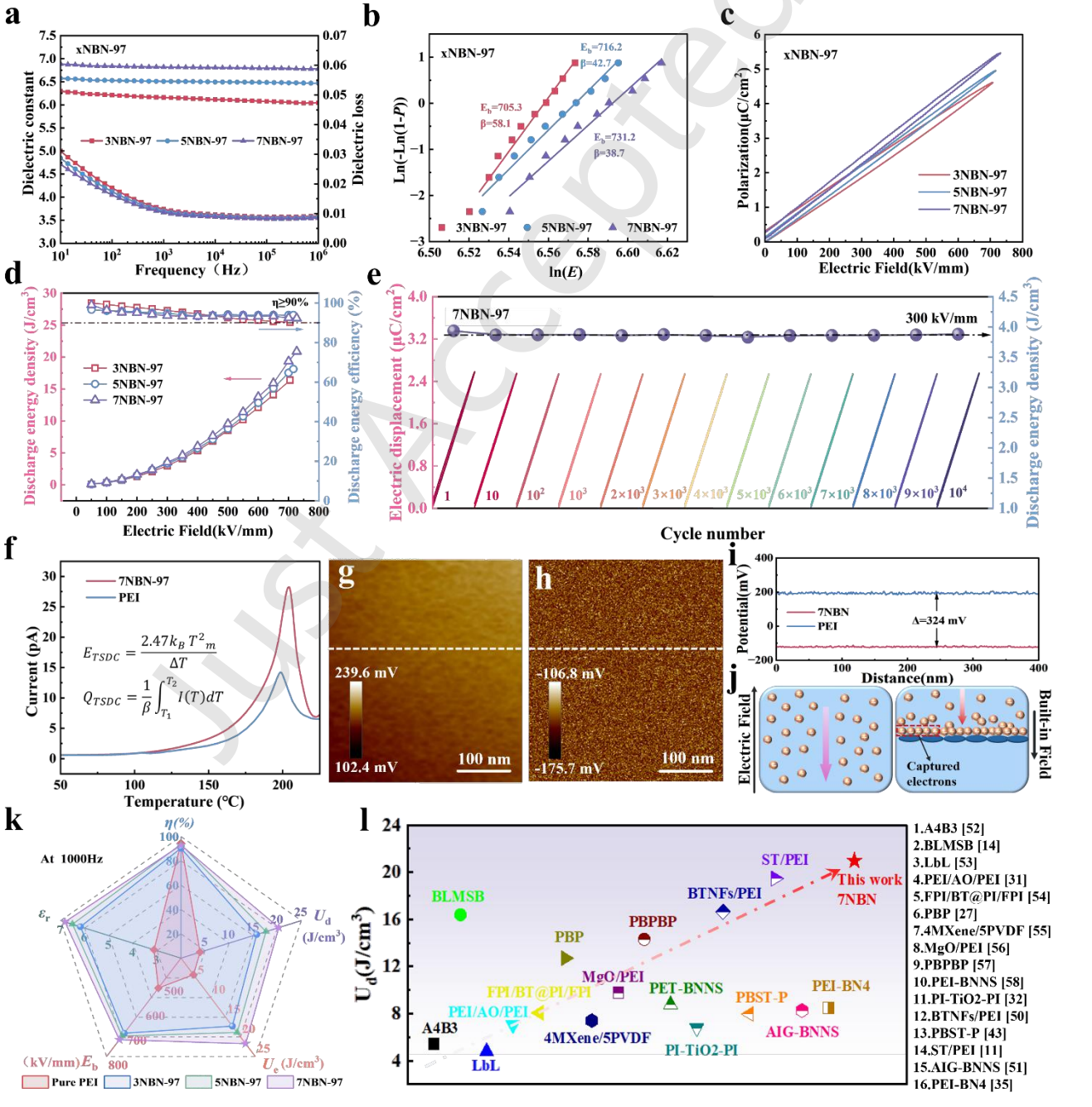

Figure 6 Dielectric constants and dielectric loss of (a) xNBN-97. (b) Weibull distribution of E_b for multilayer composites. (c)P-E loops. (d)

U_d and η of multilayer composites. (e) Cyclic stability and corresponding P-E loops of 7NBN-97 at 300 kV·mm^{-1}. (f) TSDC curves of PEI and 7NBN-97. Surface potential and corresponding morphology of (g) PEI and (h) 7NBN-97 films. (i) The difference in surface potential between PEI and 7NBN-97 films. (j) Schematic diagram of the built-in electric field in composite materials. (k) Comparison of properties of PEI, 3NBN-97, 5NBN-97 and 7NBN-97. (l) Compared with other multilayer films.

Finite element simulation results further confirm the regulation effect of the multilayer structure on electric field and potential distribution [47]. Numerical simulations of the potential distribution in neat PEI and NBN films with different layer numbers under an applied electric field of 400 kV·mm^{-1} (Figs. 4(g)-4(j) and Figure S22) reveal that as the number of alternating layers increases, the internal electric field distribution becomes more uniform, and local field distortion is gradually weakened. Among all samples, 7NBN exhibits the weakest degree of electric field concentration. Notably, in the inner CPEI@BST/PEI functional region, the electric field gradient changes more smoothly, which indicates that the alternating multilayer structure effectively mitigates dielectric constant mismatch between different layers and suppresses local field enhancement at interlayer interfaces. These results demonstrate that the rational design of multilayer dielectrics enables active regulation of the internal electric field distribution, which underlies the enhanced E_b and provides a feasible strategy for further improving energy storage performance.

To systematically investigate the influence of the multilayer structure on energy storage performance, polarization-electric field (P-E) hysteresis loops were measured for 3NBN composite films with various compositions (Figs. 5(e), 5(f) and Figures S23, S24). Under applied electric fields below the E_b, the polarization intensity increases almost linearly with the electric field, and the hysteresis loops exhibit a small enclosed area with negligible hysteresis, which is consistent with the intrinsic linear dielectric behavior of the PEI matrix. As the loading of CPEI@BNNS and CPEI@BST increases, the maximum polarization intensity (D_{max}) is significantly enhanced, indicating that the multilayer composites exhibit a stronger polarization response under an external electric field. With total filler content increasing from 0 to 11 wt%, D_{max} increases from 1.51 μC·cm^{-2} (neat PEI) to 4.65 μC·cm^{-2} for the 3NBN-xx series (Figure S25). This polarization enhancement originates from the synergistic effect of the multilayer functional architecture: the inner CPEI@BST/PEI functional layer, with its high intrinsic permittivity, generates strong polarization under an applied electric field, serving as the primary source of polarized charges; the outer CPEI@BNNS/PEI barrier layer leverages the superior insulation and high-aspect-ratio two-dimensional structure of BNNS to create efficient charge barriers and deep traps, effectively blocking carrier injection, capturing migrating charges, and suppressing conductive loss; additionally, the alternating multilayer architecture introduces numerous planar interfaces with significant dielectric contrast between the high-dielectric BST layers and the high-insulation BNNS layers, inducing strong interfacial polarization that further enhances the overall polarization intensity of the composite. When the CPEI@BST content is fixed at 7 wt%, the maximum polarization intensity reaches 4.61 μC·cm^{-2} at a CPEI@BNNS loading of 9 wt% (Figure S26), confirming that this filler ratio enables the composite film to store more charge under an applied electric field and achieve superior energy storage capacity. The discharge energy density (U_d) and charge-discharge efficiency (η) were estimated from the P-E hysteresis loops (Figs. 5(i)–5(l)). The maximum U_d of the 3NBN-xx series reaches 13.87 J·cm^{-3}, while the 3NBN-x7 series achieves 16.38 J·cm^{-3}, which is 3.85 times that of neat PEI. Furthermore, the energy efficiency remains above 90% across the entire tested electric field range. This outstanding performance results from the synergistic effects of composition optimization and structural design: the incorporation of modified BNNS and BST enhances both the dielectric constant and E_b, while the ordered alternating multilayer structure homogenizes the internal electric field and suppresses leakage current loss, thereby simultaneously improving energy storage density and efficiency.

Drawing on the above results, the optimal energy storage performance of the 3NBN composite film is achieved at CPEI@BNNS and CPEI@BST loadings of 9 wt% and 7 wt%, respectively. Using this filler ratio, five-layer (5NBN-97) and seven-layer (7NBN-97) alternating multilayer films were fabricated via the spray-based layer-by-layer assembly strategy, and the effect of layer number on dielectric and energy storage properties was systematically investigated. Fig. 6(a) shows the frequency dependent permittivity and dielectric loss of the xNBN-97 series. All samples exhibit excellent frequency stability of the permittivity. The permittivity of 7NBN-97 reaches 7.43 at 1 kHz (Figure S27). Dielectric loss decreases slightly with increasing frequency and remains below 0.03 over the entire tested frequency range, indicating excellent low-loss characteristics. A two-parameter Weibull distribution was again utilized to analyze the E_b and β (Fig. 6(b)). E_b gradually increases with increasing layer number, and all multilayer samples exhibit E_b >700 kV·mm^{-1}. Among them, 7NBN-97 achieves the maximum E_b of 731.2 kV·mm^{-1}. The improvement in E_b with increasing layer number (at constant total film thickness) is attributed to the following structural optimizations: as the layer number increases from 3 to 7, the thickness of each individual layer decreases. During the spraying process, the CPEI@BNNS in the insulating layers achieves better in-plane orientation and more uniform dispersion, which effectively reduces penetrating pore defects. The reduced thickness of the CPEI@BST layers inhibits the formation of continuous low-breakdown-strength conductive paths. Meanwhile, the interfacial density of the

composite increases greatly, which significantly enhances the charge blocking effect at interlayer interfaces. This conclusion is supported by leakage current tests (Figure S21), which show a clear monotonic decrease in leakage current density with increasing layer number. Furthermore, as shown in Fig. 6(c) and Figure S28, the maximum polarization intensity under a high electric field also increases with increasing layer number, rising from 4.61 μC·cm^{-2} (3NBN-97) to 5.46 μC·cm^{-2} (7NBN-97) (Figure S29). This enhanced polarization is attributed to the abundant Maxwell–Wagner–Sillars (MWS) interfaces formed between the low-dielectric CPEI@BNNS layers and the high-dielectric CPEI@BST layers in the alternating multilayer architecture [48]. Due to the distinct conductivity and dielectric constant of the two phases, charges accumulate at the interlayer interfaces under an external electric field, inducing intense interfacial polarization that enhances the overall polarization intensity of the composite. With the synergistic improvement in E_b and dielectric constant achieved by increasing the layer number, the energy storage properties of xNBN-97 composite films is further enhanced. As shown in Fig. 6(d), the maximum U_d of 7NBN-97 reaches 20.87 J·cm^{-3}, which is 4.91 times that of neat PEI (4.25 J·cm^{-3}), and the energy efficiency remains above 90% over the entire tested electric field range (Figure S30). Cyclic stability tests (Fig. 6(e)) demonstrate that after 10^4 continuous charge-discharge cycles at 300 kV·mm^{-1} and room temperature, 7NBN-97 maintains excellent energy storage stability, ensuring long-term reliability for practical capacitor devices. These superior dielectric energy storage properties confirm that the ultrathin alternating multilayer structure enables functional partitioning and synergistic electric field regulation of high-insulation and high-polarization phases at the nanoscale, effectively breaking the traditional trade-off between dielectric constant and breakdown strength in single-layer composite dielectrics. This work also provides a feasible and innovative strategy for designing high-performance energy-storage dielectric materials [21].

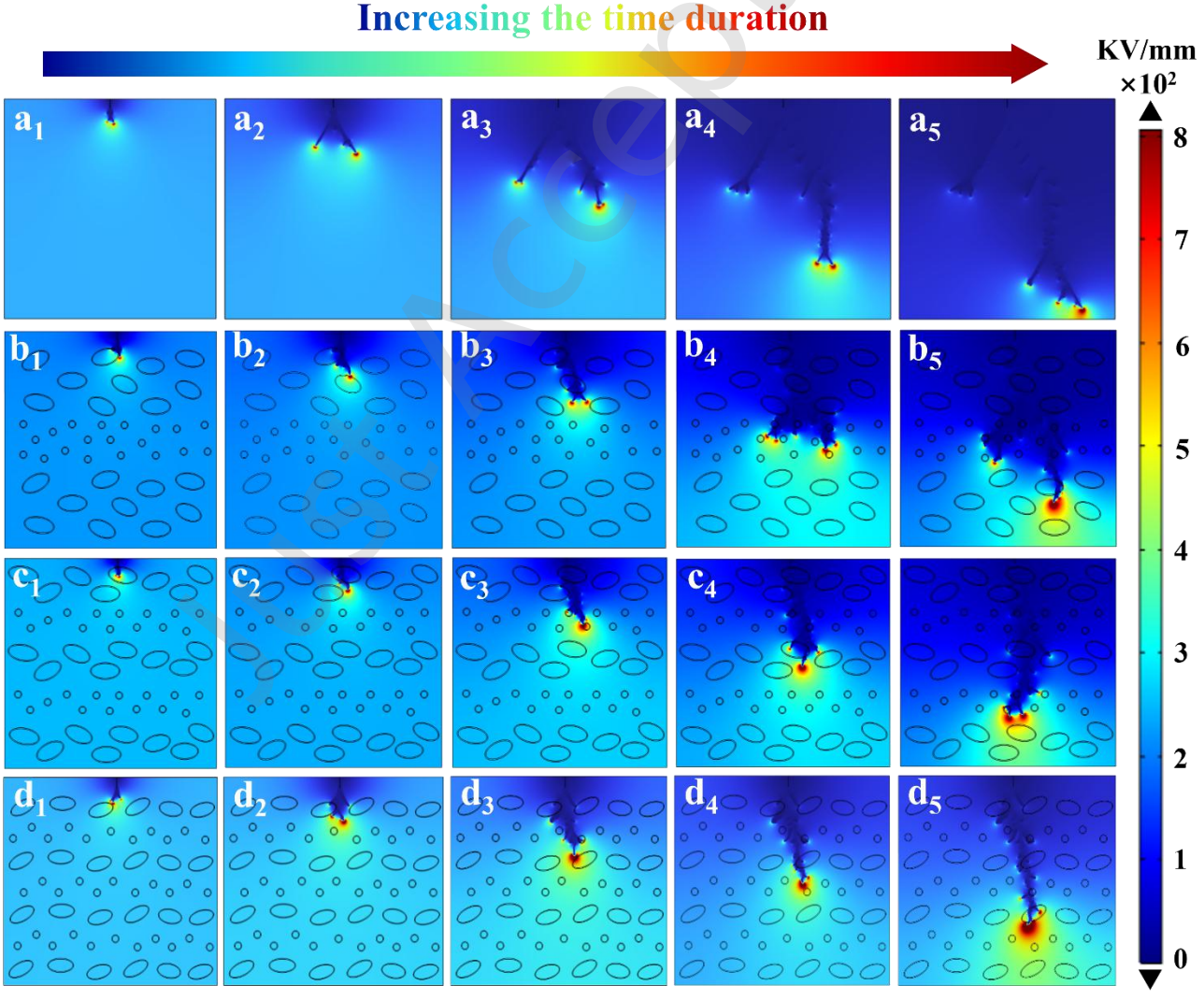

Figure 7 (a_1–a_5) Electrical tree evolution for PEI. (b_1–b_5) Electrical tree evolution for 3NBN-97. (c_1–c_5) Electrical tree evolution for 5NBN-97. (d_1–d_5) Electrical tree evolution for 7NBN-97.

Nano Research Energy
ISSN 2791-0091 (print); 2790-8119 (online)
https://doi.org/10.26599/NRE.2026.9120269

To further clarify the intrinsic mechanism underlying the enhanced energy storage performance of the multilayer structure, in-situ characterization of the surface charge behavior of the composite films was conducted via Kelvin probe force microscopy (KPFM) [49], and the surface potential results are displayed in Figs. 6(g), 6(h). For 7NBN-97, numerous regularly arranged trap sites are formed around the CPEI@BNNS nanosheets (Fig. 6(j)), which can effectively suppress excessive accumulation of space charges at the interfaces. Compared with neat PEI, the surface potential of 7NBN-97 decreases by 324 mV (Fig. 6i), which directly confirms that the trap sites constructed by CPEI@BNNS possess highly efficient charge capture capability. Thermally stimulated depolarization current (TSDC) tests [49] were further carried out to quantitatively analyze the trap level distribution and charge capture capacity of 7NBN-97 (Fig. 6(f)). Neat PEI exhibits a peak depolarization current of only 14.21 pA at a peak temperature of 198 ℃. In contrast, 7NBN-97 delivers an increased peak depolarization current of 28.26 pA, with the peak temperature rising to 204 ℃. These results demonstrate that the ultrathin multilayer structure can induce the creation of deeper trap energy levels and higher trap density, which is conducive to trapping more migrating charges. Quantitative fitting of the TSDC curves was performed to obtain the average trap energy level (E_{TSDC}) and total trapped charge quantity (Q_{TSDC}). Compared with neat PEI, which has E_{TSDC}=1.89 eV and Q_{TSDC}=3.62 nC, 7NBN-97 presents superior trap regulation performance with a deeper average trap level of 2.37 eV and a higher total trapped charge of 5.83 nC.

The above results confirm that the ultrathin alternating multilayer structure increases both the total trap density and the proportion of deep-level traps, thereby enhancing the capture and confinement of free carriers-this is the key microscopic mechanism for the high energy storage density of 7NBN-97. In addition, COMSOL multiphysics simulation was adopted to systematically simulate the dynamic evolution process of electrical tree breakdown in neat PEI and xNBN multilayer composite films (Note S3, ESM) [50, 51]. The simulation results (Fig. 7) show that under the sustained local field concentration at the tree tip, electrical trees initiate from the electrode tip and propagate inward. Neat PEI exhibits the fastest growth rate, forming dense dendritic networks that are typical of brittle breakdown. In contrast, the alternating multilayer structure effectively suppresses tree growth; as the layer number increases from 3 to 7, both the growth rate and branch length of electrical trees decrease. 7NBN-97 (Figs. 7(d_1)-7(d_5)) shows the best inhibition effect: the electrical tree remains mostly a single trunk with many short branches, which effectively delays the final breakdown. This improvement originates from the synergistic effect of abundant interlayer interfaces and sheet-like fillers: on one hand, heterogeneous interlayer interfaces act as physical barriers, blocking and deflecting the propagation of electrical trees; on the other hand, both BNNS and BST fillers disperse local electric field concentrations at the electrode tip and tree head, suppressing the initiation and growth of electrical trees. As shown in Figure S31, the equipotential lines become more regular and continuous with increasing layer number, and the field concentration zone at the tree tip shrinks. In 7NBN-97, potential variation is confined mainly to the main trunk of the electrical tree, and equipotential bending only occurs at the branch positions. This results from the combined effect of interfaces and fillers: interfaces hinder the expansion of electrical trees, while fillers alleviate local field aggregation, leading to stable equipotential evolution and significantly delayed dielectric breakdown.

The radar chart (Fig. 6(k)) and Table S1, S2 compare the comprehensive performance of neat PEI, 3NBN-97, 5NBN-97, and 7NBN-97. At a fixed total film thickness, 7NBN-97 exhibits superior energy storage performance with increased layer number. This improvement originates from multi-level structural optimization: the reduced single-layer thickness enhances the in-plane orientation of BNNS and restricts the size of ferroelectric domains and continuous leakage paths in BST layers; meanwhile, the increased interfacial density improves defect dispersion and thermal management capability. Consequently, the breakdown strength is greatly enhanced, and the overall polarization is strengthened by the synergy between the intrinsic ferroelectric polarization of BST and the interlayer interfacial polarization, enabling simultaneous increases in dielectric constant and breakdown strength. Owing to its outstanding comprehensive properties, 7NBN-97 achieves a discharge energy density that is superior to most multilayer polymer composite dielectrics reported in recent literature [11, 14, 27, 31, 32, 35, 43, 50-58] (Fig. 6(l)). Notably, the spray-based layer-by-layer assembly method employed in this work enables precise control of the layer number simply by adjusting the slurry concentration and dosage per spraying step while maintaining a fixed total film thickness. As a result, it is expected to further enhance the energy storage performance of the multilayer composite film by preparing thinner single layers under the condition of maintaining the same total thickness, which can introduce more interfaces and optimize the internal electric field distribution. Therefore, the proposed spray-based layer-by-layer assembly strategy offers important theoretical guidance and a feasible technical route for designing high-energy-density polymer composite dielectrics, with promising applications in pulsed power devices and capacitor energy storage systems.

4 Conclusions

In conclusion, we have designed a novel and controllable layer-by-layer spray assembly strategy, synergistically integrating structural ordering and interface engineering, to fabricate high-performance multilayer polymer-based dielectric composites. Carboxylated polyetherimide (CPEI),

structurally homologous to the PEI matrix, was molecularly designed and grafted onto BNNS and BST fillers. Multiscale characterizations (XRD, FTIR, XPS, TGA, SEM) confirmed successful grafting modification of fillers, and exceptional interfacial integrity was achieved. The precise spray deposition enabled the construction of ordered alternating films with tunable layer numbers. The experimental results demonstrated that 7-layer composite (7NBN-97) exhibited a synergistic enhancement in dielectric properties, achieving a high dielectric constant (7.43), an ultrahigh breakdown strength (731.2 $kV \cdot mm^{-1}$), and a record discharge energy density of 20.87 $J \cdot cm^{-3}$—4.91 times that of pure PEI—with excellent efficiency (>90%) and cyclability. Mechanistic studies revealed that the alternating multilayer structure creates abundant deep-level interface traps that homogenize the electric field, suppress space charge, and impede electrical tree growth. This work establishes a robust and versatile platform for the systematic design and industrial scale fabrication of ultrathin dielectric films for advanced energy storage applications.

Acknowledgements

The financial support from Ministry of Science and Technology, China (MOST 2024YFB4006704) and National Natural Science Foundation of China (52503109) are gratefully acknowledged.

Declaration of conflicting interests

The authors declare no conflicting interests regarding the content of this article.

Data availability

All data needed to support the conclusions in the paper are presented in the manuscript and/or the Supplementary Materials. Additional data related to this paper may be requested from the corresponding author upon request.

Electronic Supplementary Material: Supplementary materials (experimental details; material characterization; mechanical and thermodynamic testing; COMSOL simulation details, etc.) are available in the online version of this article at https: //doi.org/10.26599/NRE.2026.9120269.

References

[1] Bouharras, F. E.; Raihane, M.; Ameduri, B. Recent progress on core-shell structured $BaTiO_3$@polymer/fluorinated polymers nanocomposites for high energy storage: Synthesis, dielectric properties and applications. Prog. Mater Sci. 2020, 113, 100670.

[2] Wei, R.; Liu, Y.; Gao, F.; Feng, Z.; Huo, Q.; Liu, K.; Zhang, Z.; Lei, X.; Wang, L. Enhancing high-temperature energy storage performance of poly (arylene ether nitrile) hybrids synergistically via phthalonitrile modified boron nitride and carbon nanotube. Adv. Compos. Hybrid Mater. 2024, 7,50.

[3] Shi, Z.; Thomas, S.; Tian, Z.; Guo, D.; Zhao, Z.; Wang, Y.; Li, S.; Wehbe, N.; Emwas, A.-H.; Bakr, O. M. et al. A tailored highly solvating electrolyte toward ultra lean-electrolyte Li–S batteries. Nano Res. Energy 2024, 3, e9120126.

[4] Su, Z.; Huang, Q.; Guo, Q.; Hoseini, S. J.; Zheng, F.; Chen, W. Metal–organic framework and carbon hybrid nanostructures: Fabrication strategies and electrocatalytic application for the water splitting and oxygen reduction reaction. Nano Res. Energy 2023, 2, e9120078.

[5] Zhang, Z.; Zhou, L.; Wang, L.; Hao, Q.; Hua, X.; Wei, R. Enhancing energy storage density of poly (arylene ether nitrile) via incorporating modified barium titanate nanorods and hot-stretching. Nano Res. 2024, 17, 7574-7584.

[6] Gao, Y.; Song, Z.; Hu, H.; Mei, J.; Kang, R.; Zhu, X.; Yang, B.; Shao, J.; Chen, Z.; Li, F. et al. Optimizing high-temperature energy storage in tungsten bronze-structured ceramics via high-entropy strategy and bandgap engineering. Nat. Commun. 2024, 15, 5869.

[7] Tan, X.; Chu, K.; Chen, Z.; Han, N.; Zhang, X.; Pan, H.; Guo, W.; Chen, G.; Ni, B.-J.; Zhou, Z. et al. Recent advances in self-healing hydrogel composites for flexible wearable electronic devices. Nano Res. Energy 2024, 3, e9120123.

[8] Liu, Y.; Feng, Z.; Dang, Z.; Hou, Q.; Yu, Y.; Zhao, X.; Wang, L.; He, Y.; Wei, R.; Hua, X. Quaternary ammonium and copper phthalocyanine functionalized polyurea heterogeneous catalysts for CO_2 and epoxides cycloaddition. Chin. J. Chem. Eng. 2026, 90, 157-167.

[9] Huang, X.; Li, Y.; Zhu, W.; Li, X.; Sun, J.; Zeng, S.; Shi, S.; Cheng, F.; Wu, Y. Assembly of Bone-Inspired Cellulose-Based Dielectric Materials with Highly Oriented Structures and Superior Dielectric Properties toward Advanced Energy Storage. ACS Nano 2026, 20, 5675-5686.

[10] Jiang, Z.-H.; Li, W.-D.; Yang, X.; Chen, X.; Wang, C.; Chen, M.-Y.; Zhang, G.-J. Low dielectric loss and high breakdown strength photosensitive high-k composites containing perfluoroalkylsilane treated $BaTiO_3$ nanoparticles. Compos. Part B Eng. 2020, 192, 108013.

[11] Jin, Z.; Lin, Y.; Wang, Y.; Yang, H. Sandwich-structured $SrTiO_3$/PEI composite films with high-temperature energy storage performance. J. Power Sources 2024, 609, 234677.

[12] Zhang, Q.; Xie, Q.; Wang, T.; Huang, S.; Zhang, Q. Scalable all polymer dielectrics with self-assembled nanoscale multiboundary exhibiting superior high temperature capacitive performance. Nat. Commun. 2024, 15, 9351.

[13] Lin, J.; Wu, X.; Xia, Y.; Nie, L.; Zuo, P.; Mi, P.; Zhuang, Q. The poly (arylene ether urea) double interface layer formed in PEEU@HfO_2/PEI nanocomposites enables enhanced dielectric and energy storage performance. Surf. Interfaces 2024, 49, 104462.

[14] Dang, Z.; Lin, Y.; Yuan, Q.; Li, X.; Zhang, Y.; Ma, Y.; Wang, Y.; Yang, Q.; Wang, Y.; Yang, H. Ultrahigh Dielectric Energy Density and Efficiency in PEI‐Based Gradient Layered Polymer Nanocomposite. Adv. Funct. Mater. 2024, 34, 2406148.

[15] Ni, K. Y.; Zhao, W.; Bian, J.; Li, X. K.; Yang, K. C.; Jing, S. Y.; Wei, C.; Lin, H. L.; Chen, D. Q. Polyetherimide nanocomposite with enhanced mechanical, thermal and dielectric properties by incorporating synergistically exfoliated-chemical functionalization induced hexagonal boron nitride nanosheets. Polym. Compos. 2024, 45, 12256-12272.

[16] Yang, Q.; Wan, H.; Zhang, Y.; Zhang, S.; Liu, X.; Ma, R.; Xue, H. Metal organic frameworks-derived hollow functional materials: Synthetic strategies and electrocatalytic applications. Nano Res. Energy 2026, 5, e9120214.

[17] Sun, H.; Zhang, T.; Sun, H.; Yin, C.; Zhang, C.; Zhang, Y.; Zhang, Y.; Tang, C.; Chi, Q. Improved the high-temperature energy storage performance of PEI films via loading core-shell structured Al_2O_3@$BaSrTiO_3$ nanofillers. Ceram. Int. 2024, 50, 43811-43818.

[18] Wang, J.; Ma, X.; Zhang, Y.; Gong, H.; Peng, B.; Liang, S.; Xie, Y.; Wang, H. Continuous self-assembled BNNS layer on/within polymer film significantly enhances high-temperature capacitive energy storage. Energy Storage Mater. 2025, 77, 104182.

[19] Guo, Z.; Sun, Z.; Wang, P.; Bi, J.; Li, G.; Wang, J.; Sha, Y.; Shi, Z.; Qian, L. Core-double shell $Ba_{0.5}Sr_{0.5}TiO_3$@SiO_2@Polyethylene imine nanoparticles with built-in electric field toward enhancing dielectric energy storage. Compos. Sci. Technol. 2025, 264, 111107.

[20] Zhao, X.; Yang, H.; Cheng, Y.; Liu, S.; Fang, Z. Understanding of chlorine incorporation in wide-bandgap perovskites for efficient and stable solar cells. Nano Res. Energy 2025, 4, e9120172.

[21] Liu, M.; Song, J.; Qin, H.; Qin, S.; Zhang, Y.; Xia, W.; Xiong, C.; Liu, F. Significant Enhancement in Dielectric Properties of Polyimide

Alloys Through a Two-Phase Interlocking Structure. Adv. Funct. Mater. 2024, 34, 2313258.
[22] Ni, K. Y.; Li, D.; Bian, J.; Zhang, A. P.; Yang, S. K.; Yang, K. C.; Lin, H. L.; Chen, D. Q. High-temperature resistant polyetherimide dielectric nanocomposite films reinforced with polyurea-coated boron nitride nanosheets with core-shell structure. Polym. Compos. 2025, 46, S587-S601.
[23] Liu, Y.; Tang, B.; Wang, Z.; Jiao, Y.; Hou, Q.; Dang, Z.; Hua, X.; Wei, L.; Wang, L.; Wei, R. Enhanced dielectric performances of strontium barium titanate nanorod composites via improved interfacial compatibility. J. Colloid Interface Sci. 2025, 680, 85-95.
[24] Wang, W.; Yang, Y.; Qian, J.; Shi, W.; Huang, Y.; Jing, R.; Zhang, L.; Pan, Z.; Laletin, V.; Shur, V. et al. Advancing energy storage properties in barium titanate-based relaxor ferroelectric ceramics through a stagewise optimization strategy. Chem. Eng. J. 2024, 488, 151043.
[25] Wu, X.; Chen, X.; Zhang, Q. M.; Tan, D. Q. Advanced dielectric polymers for energy storage. Energy Storage Mater. 2022, 44, 29-47.
[26] Zhou, Y.; Chen, Y.; Cheng, L.; Liu, W. High‐Temperature All‐Organic Polymer Dielectrics for Capacitive Energy Storage. Adv. Mater. 2025, e13978.
[27] Yuan, M.; Ma, Y.; Yu, Q.; Tang, L.; Liu, K.; Wang, H. Synergistic Effect of Polar Phase and Hierarchical Interface Engineering on Enhancing Energy Storage Performance in BNT/PVDF Composites. Ind. Eng. Chem. Res. 2025, 64, 17259-17271.
[28] Zhang, T.; Lv, Q.; Zhang, S.; Song, M.; Li, S.; Zhang, L.; Wang, J. High-temperature energy storage performance of PEI/PVDF blends enhanced by Al_2O_3 inorganic layer depositing. J. Energy Storage 2025, 109, 115156.
[29] Zhang, X.; Shu, L.; Yang, Z.; Liu, L.; Zhu, F.; Wang, H.; Cheng, Y.-Y.-S.; Huang, Y.; Li, J.-F. Ultra-thin multilayer films for enhanced energy storage performance. Nano Energy 2024, 121, 109271.
[30] Zhang, T.; Yu, H.; Jung, Y. H.; Zhang, C.; Feng, Y.; Chen, Q.; Lee, K. J.; Chi, Q. Significantly Improved High-Temperature Energy Storage Performance of BOPP Films by Coating Nanoscale Inorganic Layer. Energy Environ. Mater. 2024, 7, e12549.
[31] Chen, X.; Wei, Y.; Wang, F.; Peng, B.; Li, X.; Hu, D.; He, G.; Yan, Z.; Luo, H.; Zhang, D. Enhanced High-Temperature Capacitive Performance of PEI Dielectrics by an Adjustable Al_2O_3 Interlayer. ACS Appl. Polym. Mater. 2024, 6, 12616-12622.
[32] Peng, S.; Wang, R.; Liang, Z.; Du, X. Significantly enhanced energy storage performance in multi-layer polyimide films with nano dielectric layer. J. Energy Storage 2024, 99, 113381.
[33] Wei, R.; Jiao, Y.; Liu, Y.; Wang, Z.; Zhao, X.; Bao, S.; Wang, L.; Dang, Z. M.; Zheng, X.; Hua, X. Hot stretching induced Orientation of Calcium Copper Titanate Nanorods in Polyetherimide for Enhanced Energy Storage Density. Small 2025, 22, e13033.
[34] Wei, R.; Wang, Z.; Jiao, Y.; Liu, Y.; Bao, S.; Wang, L.; Hua, X.; Wang, X. Enhancing Dielectric Energy Storage Properties of Poly(Arylene Ether Nitrile) Via Controlling the Distribution of Boron Nitride Nanosheets. Adv. Funct. Mater. 2025, 36, e19368.
[35] Ba, Z.; Ma, L.; Liu, H.; Li, C.; Chen, X.; Wen, X.; Song, P.; Lei, Q. Bio-inspired PEI/BNNS composite film via hydrogen bond self-assembly for efficiently enhancing high-temperature dielectric energy storage. Compos. Commun. 2025, 54, 102266.
[36] Miao, W.; Chen, H.; Pan, Z.; Pei, X.; Li, L.; Li, P.; Liu, J.; Zhai, J.; Pan, H. Enhancement thermal stability of polyetherimide-based nanocomposites for applications in energy storage. Compos. Sci. Technol. 2021, 201, 108501.
[37] Wu, L.; Wu, K.; Liu, D.; Huang, R.; Huo, J.; Chen, F.; Fu, Q. Largely enhanced energy storage density of poly(vinylidene fluoride) nanocomposites based on surface hydroxylation of boron nitride nanosheets. J. Mater. Chem. A 2018, 6, 7573-7584.
[38] Zuo, P.; Jiang, J.; Wang, R.; Chen, D.; Lin, J.; Chen, Y.; Wang, X.; Zhuang, Q. Poly(ether imide) Nanocomposites with $BaTiO_3$@TiO_2@SiO_2 or $BaTiO_3$@SiO_2@TiO_2 Fillers Improve Energy Storage Capacity and Dielectric Thermal Stability. ACS Appl. Nano Mater. 2023, 6, 18381-18393.
[39] Yang, F.; Bao, Y.; Zeng, B.; Wu, J.; Li, X.; Sun, Y.; Chen, Y.; Wang, G. Excellent energy storage properties in ZrO_2 toughened $Ba_{0.55}Sr_{0.45}TiO_3$-based relaxor ferroelectric ceramics via multi-scale synergic regulation. Chem. Eng. J. 2024, 493, 152624.
[40] Chun, H.-J.; Lee, Y.; Kim, S.; Yoon, Y.; Kim, Y.; Park, S.-C. Surface Termination of $BaTiO_3$(111) Single Crystal: A Combined DFT and XPS Study. Appl. Surf. Sci. 2022, 578, 152018.
[41] Lefebvre, J.; Galli, F.; Bianchi, C. L.; Patience, G. S.; Boffito, D. C. Experimental methods in chemical engineering: X-ray photoelectron spectroscopy-XPS. Can. J. Chem. Eng. 2019, 97, 2588-2593.
[42] Slimani, Y.; Selmi, A.; Hannachi, E.; Almessiere, M. A.; AlFalah, G.; AlOusi, L. F.; Yasin, G.; Iqbal, M. Study on the addition of SiO_2 nanowires to $BaTiO_3$: Structure, morphology, electrical and dielectric properties. J. Phys. Chem. Solids 2021, 156, 110183.
[43] Jaidka, S.; Singh, D. P. Tailored multilayered films of the PVDF/$Ba_{0.8}Sr_{0.2}TiO_3$ nanocomposites with surface-modified nanoparticles for superior dielectric and energy storage performance. J. Alloys Compd. 2024, 1003, 175468.
[44] Ren, L.; Guo, K.; Cui, R.; Wang, X.; Zhang, M.; Deng, C. Excellent energy storage performance in BSFCZ/AGO/BNTN double-heterojunction capacitors via the synergistic effect of interface and dead-layer engineering. Nano Energy 2024, 129, 110065.
[45] Meng, Z.; Zhang, T.; Zhang, C.; Dang, Z. M.; Chi, Q. Optimizing Energy Storage Performance in Polymer Dielectrics through Dual Strategies: Constructing "Peaked" Barrieras and Enhancing Carrier Scattering. Adv. Funct. Mater. 2024, 34, 2403402.
[46] Lu, T.; Chen, F. Multiwfn: A multifunctional wavefunction analyzer. J. Comput. Chem. 2012, 33, 580-592.
[47] Gao, F.; Zhou, L.; Liu, K.; Feng, Z.; Huo, Q.; Yang, C.; Zhang, T.; Mao, Y.; Li, D.; Wang, L. et al. Improving energy storage properties of polyarylene ether nitrile with coral-like $CaCu_3Ti_4O_{12}$ nanorods. Chem. Eng. J. 2024, 493, 152830.
[48] Huang, B.; Yu, Y.; Zhao, Y.; Zhao, Y.; Dai, L.; Zhang, Z.; Fei, H.-F. Al@SiO_2 Core–Shell Fillers Enhance Dielectric Properties of Silicone Composites. ACS Omega 2023, 8, 35275-35282.
[49] Yin, P.; Lei, L.; Tang, Q.; Dastan, D.; Liu, Y.; Wang, H.; Shi, Z. Polymer dielectrics intercalated with a non-contiguous granular nanolayer for high-temperature pulsed energy storage. Energy Storage Mater. 2025, 77, 104213.
[50] Yuan, Q.; Wei, L.; Wang, Y.; Ma, Y.; Li, Y.; Wang, Y.; Yang, H. Enhanced capacitive energy storage performance induced by incorporating $BaTiO_3$ nanofibers in PEI-based multilayered nanocomposite films. J. Energy Storage 2025, 137, 118588.
[51] Yue, D.; Zhang, W.; Wang, P.; Zhang, Y.; Teng, Y.; Yin, J.; Feng, Y. Constructing asymmetric gradient structures to enhance the energy storage performance of PEI-based composite dielectrics. Mater. Horiz. 2024, 11, 726-736.
[52] Li, S.; Qu, J.; Wang, J.; Li, X.; Dai, X.; Jiang, Y.; Shen, Z.; Li, B.-W.; Zhang, X. Scalable multilayered dielectric polymer film exhibiting significantly improved high-temperature energy density. Surf. Interfaces 2024, 51, 104632.
[53] Lv, W.; Weng, Y.; Wang, Y.; Guo, M.; Sha, X.; Cao, Z.; Liu, Y.; Lu, H.; Xu, R.; Li, Q. et al. Integration of Interfacial Chemistry-Guided BaTiO3 Nanoparticle Arrangements in Polymer Film Stacks for Pressure-Sensing Devices. ACS Nano 2025, 19, 34819-34829.
[54] Zhu, L.; Yuan, P.; Kou, X.; Jing, B.; An, W.; Ma, R.; Hu, D. Fluorinated polyimide/barium titanate@polyimide/fluorinated polyimide sandwich nanocomposite film capacitors for high-temperature energy storage and piezoelectric sensing. Colloids Surf. A 2025, 727, 138360.
[55] Li, W.; Song, Z.; Zhong, J.; Qian, J.; Tan, Z.; Wu, X.; Chu, H.; Nie, W.; Ran, X. Multilayer-structured transparent MXene/PVDF film with excellent dielectric and energy storage performance. J. Mater. Chem. C 2019, 7, 10371-10378.
[56] Zhang, N.; Zhang, C.; Guo, H.; Bai, J.; Zhao, H. Superior high-temperature energy storage performance of Polyetherimide-Based dielectric composites via optimization of the spatial distribution of MgO nanoparticles. Chem. Eng. J. 2025, 508, 161058.
[57] Zhu, Y.; Shen, Z.; Li, Y.; Chai, B.; Chen, J.; Jiang, P.; Huang, X. High Conduction Band Inorganic Layers for Distinct Enhancement of Electrical Energy Storage in Polymer Nanocomposites. Nano-Micro Lett. 2022, 14, 151.

[58] Ping, J.-B.; Feng, Q.-K.; Zhang, Y.-X.; Wang, X.-J.; Huang, L.; Zhong, S.-L.; Dang, Z.-M. A Bilayer High-Temperature Dielectric Film with Superior Breakdown Strength and Energy Storage Density. Nano-Micro Lett. 2023, 15, 154.

Renbo Wei received his Ph.D. degree from the Department of Chemical Engineering, Tsinghua University, under the supervision of Professor Xiaogong Wang, and is currently a professor at Institute of Low-Carbon Technology Application, School of Chemical Engineering, Northwest University. His research centers on the structural design of dielectric materials and low-carbon technology application.

Lingling Wang received her Ph.D. degree from School of Materials and Energy, University of Electronic Science and Technology of China under the supervision of Prof. Xiaobo Liu. Dr. Wang is currently an Associate Professor at School of Chemical Engineering, Northwest University. Her research interests mainly focus on key materials and interface issues for dielectric energy storage.

Xiufu Hua received his Ph.D. degree from the Department of Chemical Engineering, Tsinghua University, under the supervision of Professor Zheng Liu, and is currently a professor at Institute of Low-Carbon Technology Application, School of Chemical Engineering, Northwest University. His research centers on low-carbon technology application.

Electronic Supplementary Material

Fabrication of Multilayer Alternating Polymer-based Dielectric Composites with Superior Energy Storage Performance via Layer-by-layer Spraying Assembly

Renbo Wei[1], Shumin Bao[1], Yongxian Liu[1], Xiaofei Zhao[1], Yue Yu[1], Chunfang Lai[1], Lingling Wang[1] (✉), and Xiufu Hua[1,2] (✉)

[1] *Institute of Low-Carbon Technology Application, School of Chemical Engineering, Northwest University, Xi'an 710069, China*

[2] *Yangtze Delta Region Institute of Tsinghua University, Jiaxing 314006, China*

Supporting information to **https://doi.org/10.26599/NRE.2026.9120269**.

Address correspondence to Lingling Wang, wangll@nwu.edu.cn; Xiufu Hua, huaxf@nwu.edu.cn

Experimental Section

Materials

PEI was purchased from Adamas Company. Bisphenol A dianhydride (BPADA) and 3,5-diaminobenzoic acid (DBA) were obtained from Aladdin Company. Hexagonal boron nitride powder (>98%) was purchased from Suzhou Yuante New Materials Co., Ltd. Sodium hydroxide, K_2CO_3, absolute ethanol, toluene, and N-methylpyrrolidone (NMP) were supplied by Tianjin Damao Chemical Reagent Factory. N,N-dimethylacetamide (DMAc, AR) and N,N-dimethylformamide (DMF) were purchased from Tianjin Fuyu Fine Chemical Co., Ltd. Barium strontium titanate (BST) nanoparticles were obtained from Changyanke New Materials. The spray gun (Model S310) and air pump were purchased from Ustar. All reagents were of analytical grade and used without further purification.

Synthesis of Carboxylated Polyetherimide (CPEI)

In this work, CPEI was synthesized via a reported one-pot high-temperature polycondensation route (Figure S1) using BPADA and DBA as monomers. Firstly, 1.00 g of DBA and 30 mL of NMP were added sequentially into a 100 mL three-necked round-bottom flask equipped with a mechanical stirrer, thermometer and water separation reflux device, and stirred at room temperature until complete

dissolution. Afterwards, 2.60 g of BPADA was introduced into the system, and the mixture was pre-polymerized under stirring at room temperature for 4 h. Subsequently, 10 mL of toluene was added to the reaction system, and another 30 mL of toluene was supplemented into the water separator. After connecting the condenser pipe, the system was heated to 180 °C and subjected to reflux dehydration reaction for 7 h. Upon completion of the reaction, the solution was naturally cooled to room temperature. The viscous product was slowly poured into excessive absolute ethanol for precipitation. The precipitate was collected by filtration, washed three times with absolute ethanol, and dried in a vacuum oven at 80 °C for 24 h to obtain carboxyl-terminated CPEI. The nuclear magnetic resonance characterization results are presented in the supporting information (Figure S2).

Preparation of CPEI-grafted BNNS (CPEI@BNNS)

Hydroxylated boron nitride nanosheets (BNNS-OH) were fabricated via liquid-phase ultrasonic exfoliation combined with alkali hydrothermal treatment. Initially, 1.00 g of bulk hexagonal boron nitride powder was dispersed in 200 mL DMF and ultrasonically treated at room temperature for 48 h to obtain exfoliated boron nitride suspension. The suspension was centrifuged at 3000 rpm for 15 min to remove unexfoliated thick aggregates. The supernatant was further centrifuged at 10000 rpm for 10 min, and the sediment was collected and washed thoroughly with deionized water three times to eliminate residual organic solvent.The obtained exfoliated boron nitride nanosheets were dried in an oven at 80 °C for 12 h, then redispersed in 5 mol/L NaOH aqueous solution. After 1 h ultrasonic dispersion, the mixture was transferred into a Teflon-lined autoclave and maintained at 120 °C for 12 h to introduce hydroxyl active sites onto the nanosheet surface. After natural cooling, the product was collected by centrifugation and washed with deionized water until the filtrate reached neutral pH. Finally, BNNS-OH was obtained after vacuum drying at 80 °C for 12 h.

CPEI was covalently grafted onto the surface of BNNS-OH via esterification reaction. Firstly, 0.30 g of BNNS-OH was dispersed in 10 mL of DMF and ultrasonically treated for 2 h to form a homogeneous dispersion. Meanwhile, 0.20 g of CPEI was

dissolved in 20 mL of NMP under stirring at 40 °C until fully dissolved. The two solutions were mixed evenly and transferred into an autoclave, and reacted at 200 °C for 4 h to complete the esterification grafting. After the reaction, the product was centrifugally washed three times with NMP to remove unreacted free CPEI. The final product was dried in a vacuum oven at 90 °C for 12 h to obtain CPEI-modified BNNS, denoted as CPEI@BNNS.

Preparation of CPEI-grafted BST (CPEI@BST)

Two-step covalent grafting method was adopted for surface modification of BST nanoparticles. Amination pretreatment: 1.00 g of BST nanoparticles were dispersed in 150 mL absolute ethanol and stirred at room temperature for 8 h to form a uniform suspension. Subsequently, 1 mL of 3-aminopropyltriethoxysilane (KH550) was added, and the mixture was stirred at 40 °C for 16 h to introduce amino active sites on the BST surface. After reaction, the product was collected by centrifugation, washed three times with absolute ethanol to remove unreacted KH550, and dried in an air-blast oven at 70 °C for 12 h to obtain aminated BST (BST-NH_2). CPEI covalent grafting: 0.50 g of BST-NH_2 was dispersed in 20 mL NMP and stirred at room temperature for 5 h. Meanwhile, 0.30 g of CPEI was dissolved in 20 mL NMP under stirring at 40 °C. The two dispersions were well mixed and transferred into an autoclave, then reacted at 200 °C for 4 h. Covalent grafting was realized via amidation reaction between terminal carboxyl groups of CPEI and surface amino groups of BST. The product was collected by centrifugation, washed three times with NMP to eliminate free CPEI, and vacuum-dried at 90 °C for 14 h to finally obtain CPEI-grafted BST nanoparticles named CPEI@BST.

Characterization

FTIR spectra of BNNS-OH, BST-KH550, CPEI, CPEI@BNNS and CPEI@BST were measured using a BRUKER VERTEX70 TGA-IR spectrometer. The elemental compositions of BNNS-OH, CPEI@BST and CPEI@BNNS were analyzed by X-ray photoelectron spectroscopy (XPS) with a Thermo Fisher Nexsa system. The crystal structures of pristine and modified BNNS were characterized via X-ray diffraction

(XRD) on a Bruker D8 Advance diffractometer with Cu Kα radiation. The microstructures of samples were observed by SIGMA FE scanning electron microscope (SEM). The mechanical properties of NBN multilayer films were tested by a SANS CMT6104 universal tensile testing machine. A Tonghui TH2826 LCR meter was employed to measure the dielectric constant in the frequency range of $10–10^6$ Hz. Thermogravimetric analysis (TGA) was carried out on an HTG-1 instrument (Hengjiu, Beijing) under nitrogen atmosphere. Differential scanning calorimetry (DSC) tests of NBN multilayer films were performed using a DSC-1 instrument (Hengjiu, Beijing) in nitrogen flow. The breakdown strength was measured by a ZJC-50KV dielectric withstand voltage tester. Polarization-electric field (P-E) hysteresis loops were recorded at 100 Hz using a Premiere II ferroelectric tester (Radiant Technologies, Inc.). Surface potential was detected by Kelvin probe force microscopy (KPFM, Oxford Instrument Cypher ES). Thermally stimulated depolarization current (TSDC) measurements of NBN multilayer films were conducted by a Novocontrol Concept 40 broadband impedance analyzer over the temperature range from −100 °C to 230 °C.

Supplementary Note 1

The Tauc plot method

The basic principle of the Tauc plot method is to use the absorption spectrum of the semiconductor to determine the edge wavelength (also known as the absorption threshold), thereby calculating the band gap width. The specific steps and formulas are as follows:

Steps:

Obtain the absorption spectrum: First, acquire the ultraviolet-visible absorption spectrum of the material. This spectrum shows the absorption intensity of the material at different wavelengths of light.

Determine the absorption threshold: On the absorption spectrum, locate the point where the absorption intensity begins to increase significantly, which corresponds to the absorption threshold. This point corresponds to the edge wavelength (λg) of the material.

Draw the tangent: On the absorption spectrum curve, draw a tangent at the point where the curve changes most rapidly, and record the intersection of the tangent with

the x-axis as λg.

The relationship between the band gap width (E_g) and the edge wavelength (λg) can be expressed using the following formula:

$$E_g = \frac{1240}{\lambda_g (\mathrm{nm})} \quad (1)$$

In this case, 1240 is the value obtained by dividing the product of Planck's constant (h) and the speed of light (c) by the electronic charge (e)[1, 2].

Supporting Note 2

DFT Calculation

The molecular geometries of the pristine PEI and the CPEI were optimized using Density Functional Theory (DFT) Calculation[3]. The DFT calculations were performed with the DFT-B3LYP and 6-31 G basis function, as implemented the Gaussian 09 and Gauss View software. Subsequent to geometry optimization, an energy analysis of the molecular orbitals was conducted based on the optimized structure from the DFT calculations[4].

Supplementary Note 3

Comsol finite element simulation supplement (Simulation of the breakdown path)

In this study, the growth and evolution of the electrical breakdown channel were numerically simulated using the phase-field method. A rectangular domain with a size of 2cm×2cm was employed as the initial geometric model[5, 6]. To characterize the breakdown state of the material, a dimensionless phase-field variable s(x,t) was introduced, which ranges from 0to1. When s =1, the material is in an undamaged state, and when s = 0, the material is in a fully broken-down state. During the breakdown process, the dielectric constant of the material in intermediate states can be calculated using the phase-field variable s.

$$\varepsilon(s)=\frac{\varepsilon_0}{f(s)+\eta} \tag{1}$$

Here, f(s)=4s3−3s4, and η is a constant (η=0.001).

By integrating over the entire space Ω occupied by the dielectric, the system's energy function can be obtained:

$$\prod[s,\phi]=\int_\Omega[-\frac{\varepsilon(s)}{2}\nabla\phi\cdot\nabla\phi+\Gamma\frac{1-f(s)}{l^2}+\frac{\Gamma}{4}\nabla s\cdot\nabla s]dV \tag{2}$$

In the equation, Γ and Φ represent the breakdown energy and electric potential, respectively. The electrical breakdown channel forms and propagates when the electrostatic energy required per unit length to extend the breakdown channel exceeds the minimum energy needed for breakdown. The damage rate during the breakdown failure process is assumed to follow a linear kinetic law proportional to the energy driving force.

$$\frac{\partial s}{\partial t}=-m\delta\prod/\delta s \tag{3}$$

Therefore, by substituting the detailed form of the energy function, the evolution equation for the damage variable s can be derived:

$$\frac{1}{m}\frac{\partial s}{\partial t}=\frac{\varepsilon'(s)}{2}\nabla\phi\cdot\nabla\phi+\frac{\Gamma}{l^2}f'(s)+\frac{\Gamma}{2}\nabla^2 s \tag{4}$$

In this study, the damage diffusion coefficient of the composite material is characterized by the mobility m. For the convenience of numerical calculations, all lengths are normalized by l, energies are normalized by l, and time is normalized by $l^2/m\Gamma$. The electric potential is normalized by $\sqrt{(\Gamma/\varepsilon_0)}$. Consequently, the dimensionless governing equations are obtained as follows:

$$\overline{\nabla}^2\cdot\left[\frac{1}{f(s)+\eta}\right]\overline{\nabla}\overline{\varphi}=0 \tag{5}$$

$$\frac{\partial s}{\partial t}=-\frac{f'(s)}{2[f(s)+\eta]^2}\overline{\nabla\varphi}\cdot\overline{\nabla\varphi}+f'(s)+\frac{1}{2}\overline{\nabla}^2 s \tag{6}$$

The gradient energy term (∇s) is used to regularize the sharp phase boundaries, and the relative permittivity is set to the values obtained from corresponding experiments.

The governing equations are implemented in COMSOL Multiphysics 6.1, a finite element analysis software, where the PDE interface and the AC/DC module are coupled to solve for the phase-field variable and the electric potential, respectively. In our model, the voltage V between the two electrodes is applied by controlling the total charge accumulation Q on the bottom electrode, with Q increasing linearly over time as Q=It. An electric field concentrator, with a length of one-tenth of the total length, is placed at the center of the top electrode of the parallel-plate capacitor to achieve controllable field concentration and initiation of breakdown.

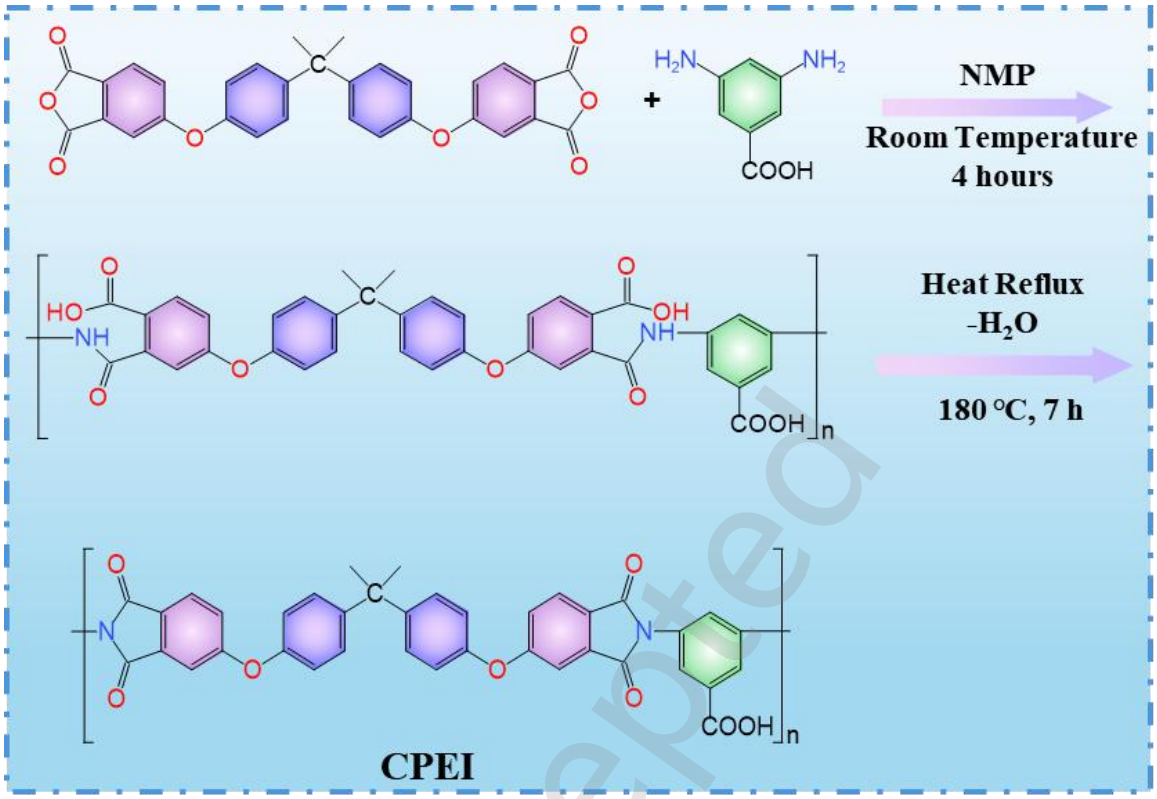

Figure S1.CPEI synthesis flow chart.

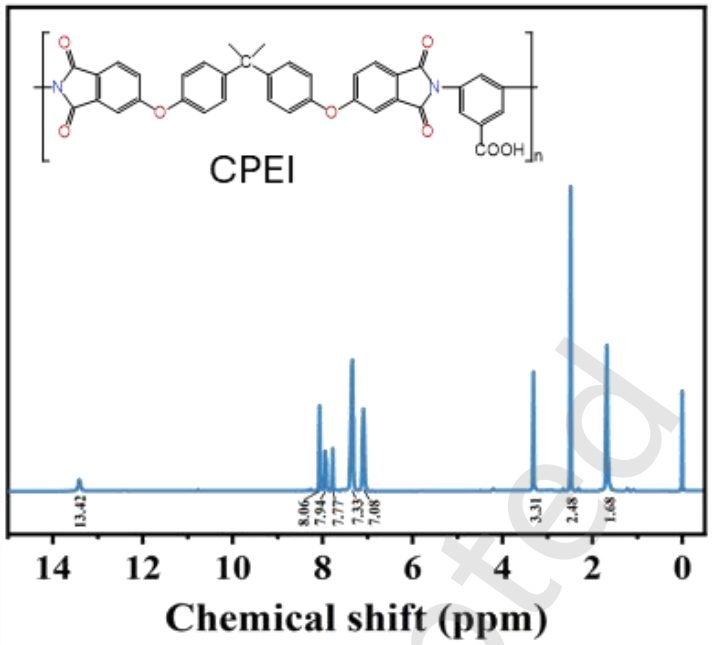

Figure S2. 1H NMR spectrum of polyetherimide containing carboxylic acid side groups.

The proton nuclear magnetic resonance (1H NMR) spectrum of cPEI is shown in the figure, with the solvent being deuterated DMSO. Analysis of the spectrum reveals that the peaks at 3.31 ppm and 2.48 ppm are due to the resonance of H2O and DMSO, respectively. The peaks in the range of 7.08-8.06 ppm are attributed to the protons of the aromatic rings in polyetherimide, with the specific assignments being 8.06 ppm for H1, 7.94 ppm for H2, 7.77 ppm for H3, 7.33 ppm for H4-H5 and H8, and 7.08 ppm for H7. Notably, there is no appearance of the proton peak from the -NH group, indicating that the polymer has undergone complete imidization reaction. The peak at 13.42 ppm is caused by the -COOH group in the side chain, and the hydrogen of the carboxyl group exhibits a large chemical shift due to the strong electronic attraction with the carbonyl.

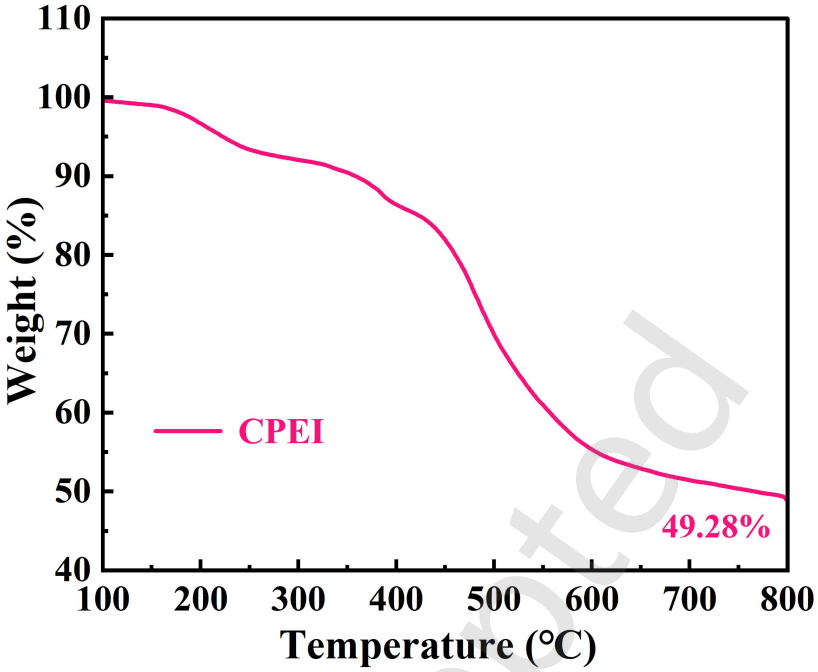

Figure S3. TGA curves of CPEI.

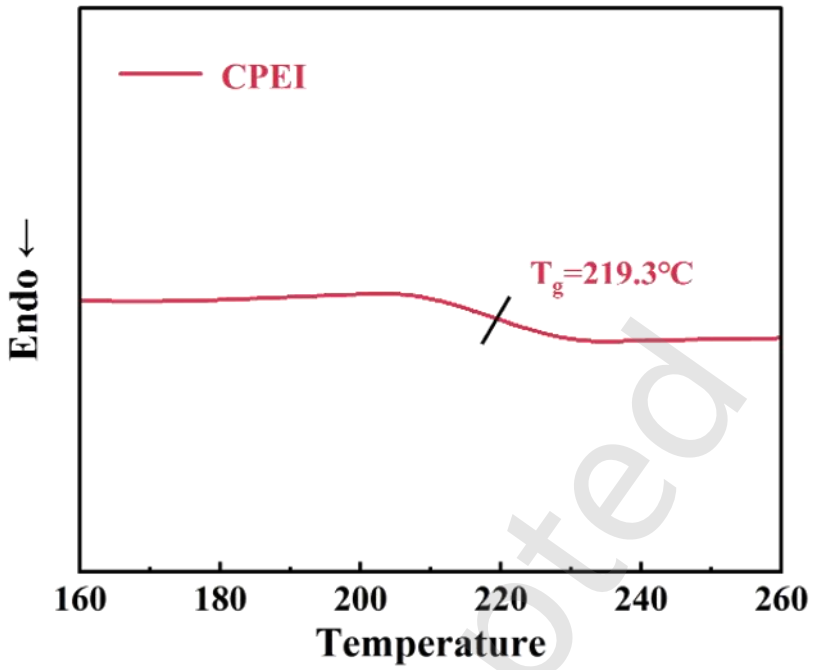

Figure S4. DSC curves of CPEI.

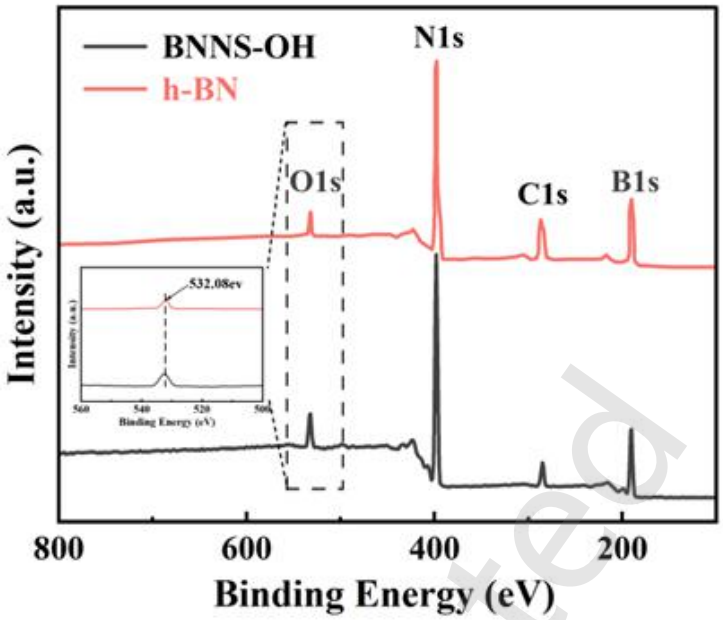

Figure S5. XPS spectra of BNNS-OH and h-BN.

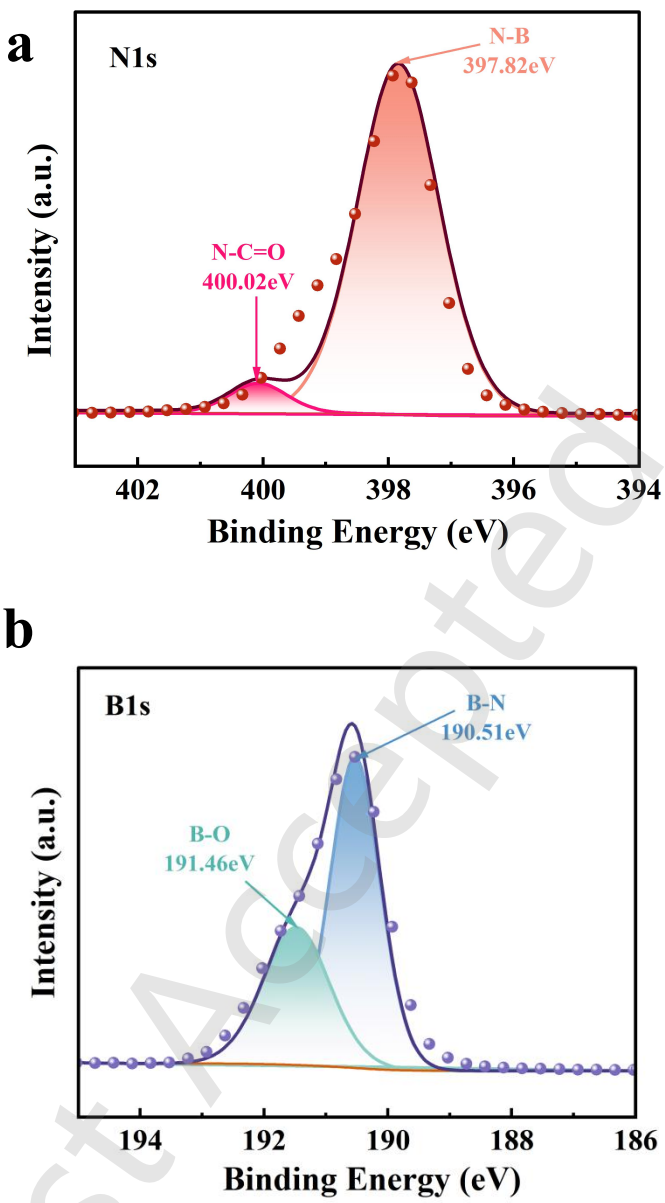

Figure S6. (a) N1s spectrum of CPEI@BNNS. (b) B1s spectrum of CPEI@BNNS.

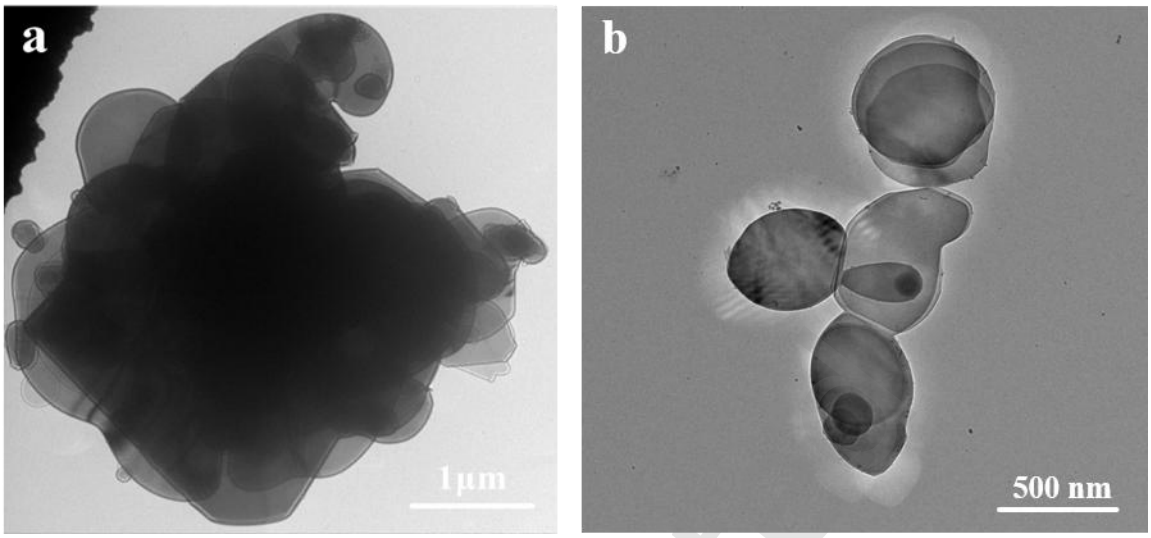

Figure S7. TEM images of (a) h-BN amd (b) BNNS.

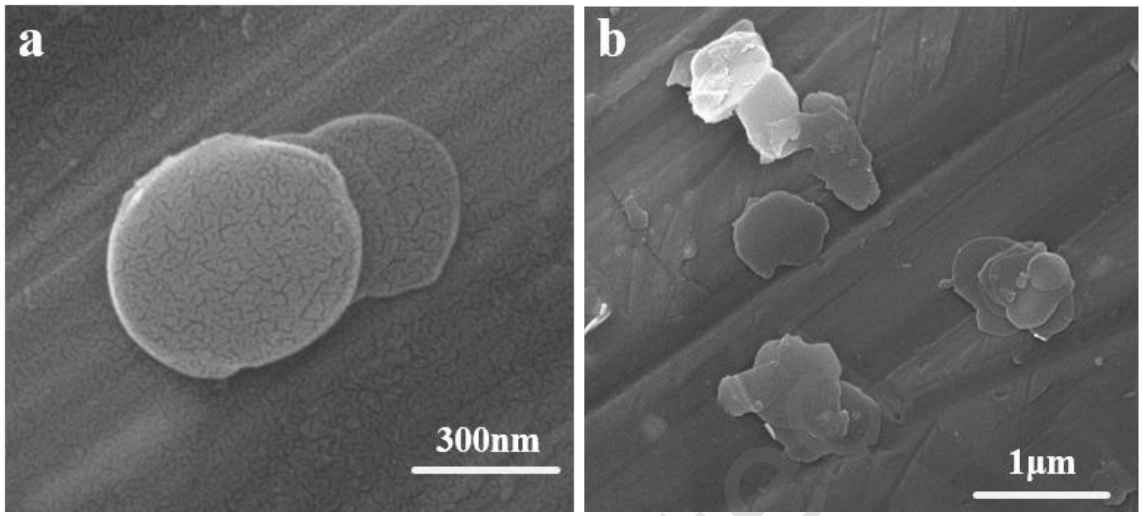

Figure S8. (a) SEM images of (a) BNNS and (b) CPEI@BNNS.

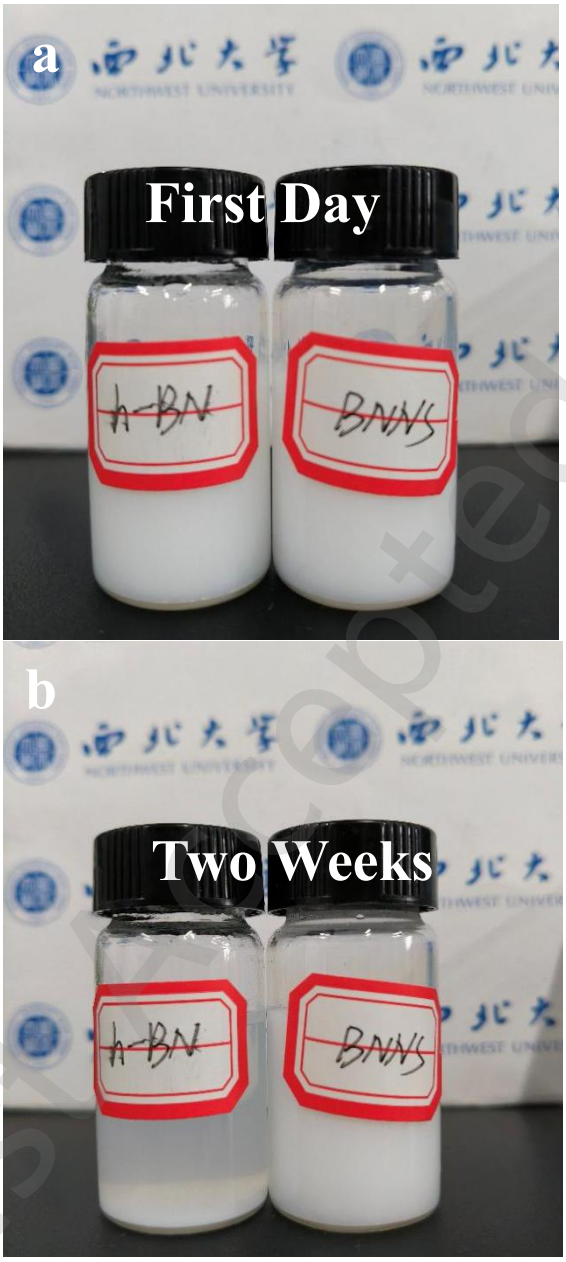

Figure S9. Physical pictures of h-BN and BNNS-OH dispersion for one day (a) and 2 weeks (b).

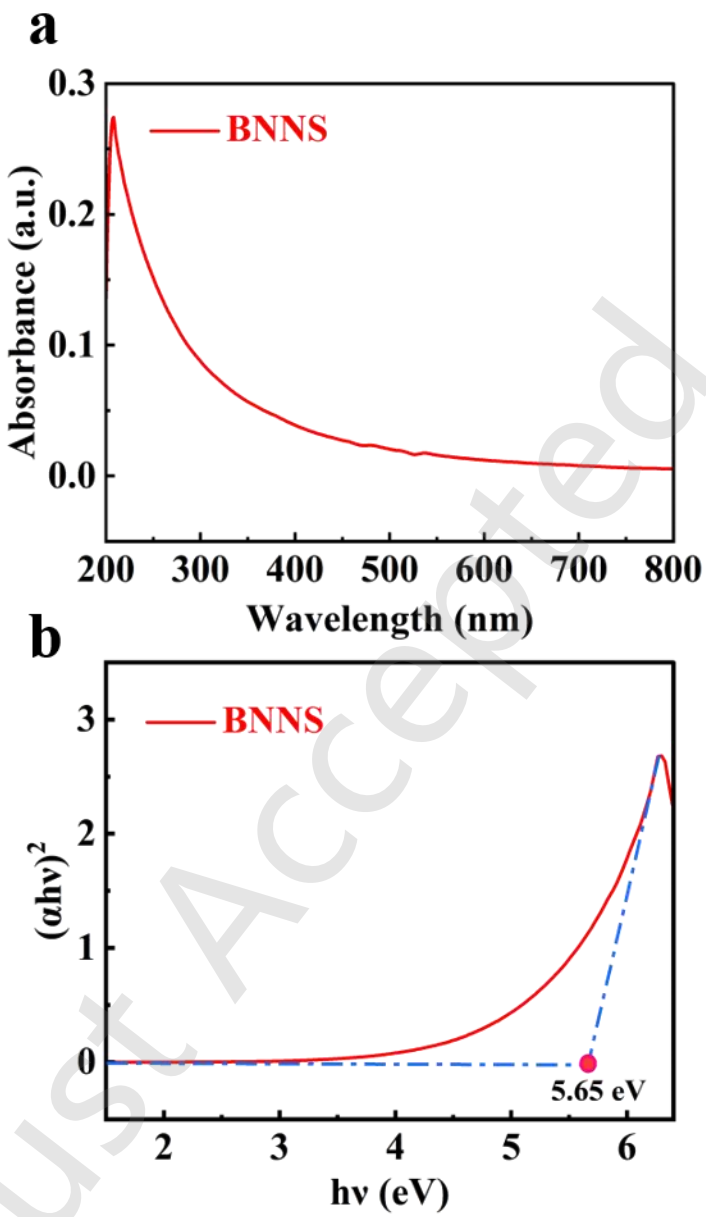

Figure S10. (a) UV-vis spectrum of BNNS. (b) the band gap of BNNS calculated by the tangent method.

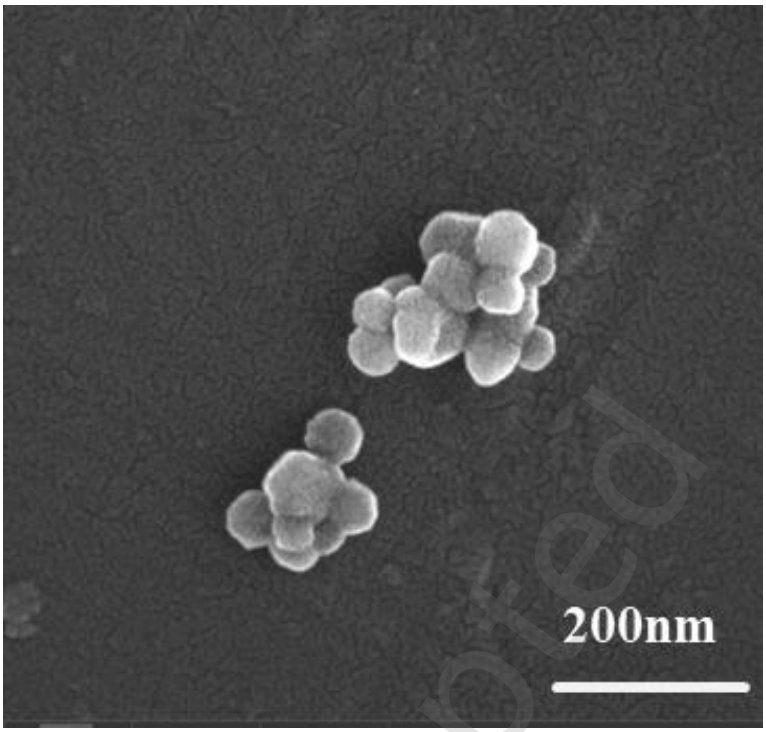

Figure S11. SEM images of CPEI@BST

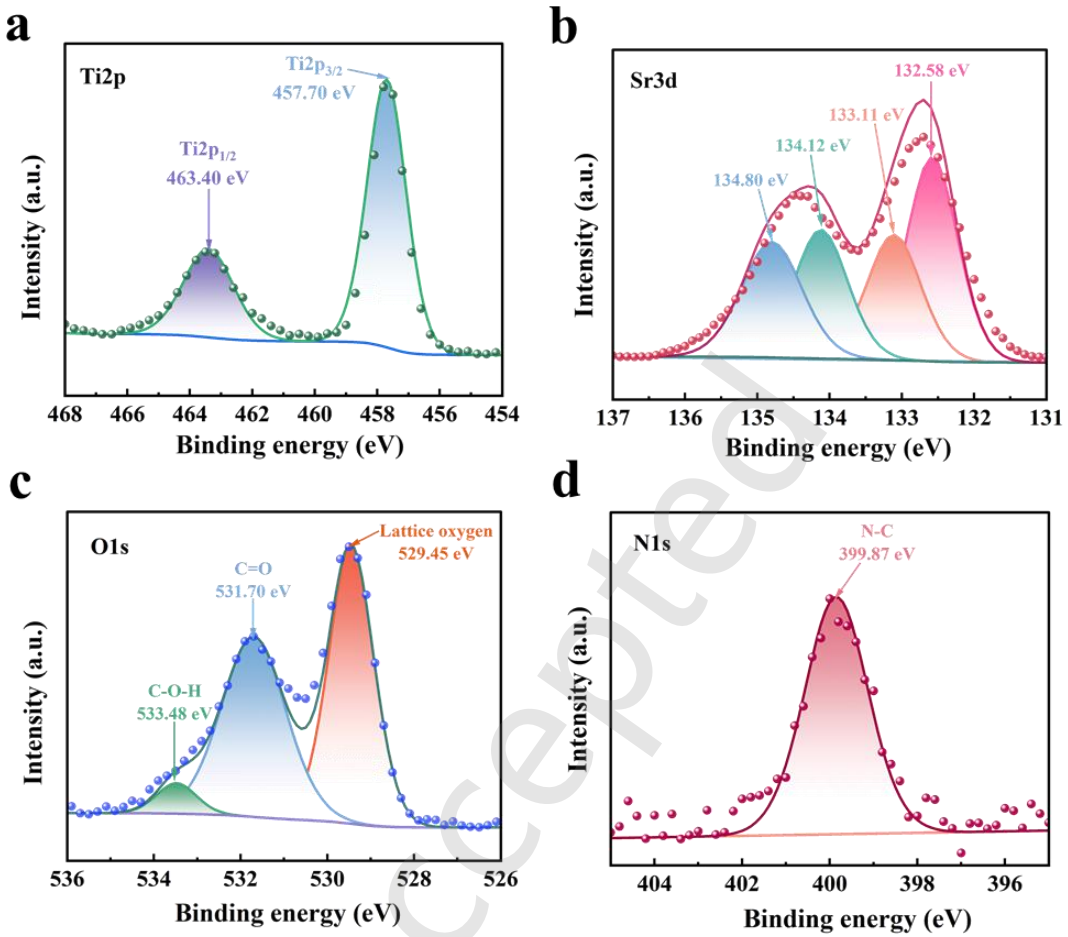

Figure S12. (a) Ti2p, (b)Sr3d, (c)O1s, (d)N1s spectrum of CPEI@BST.

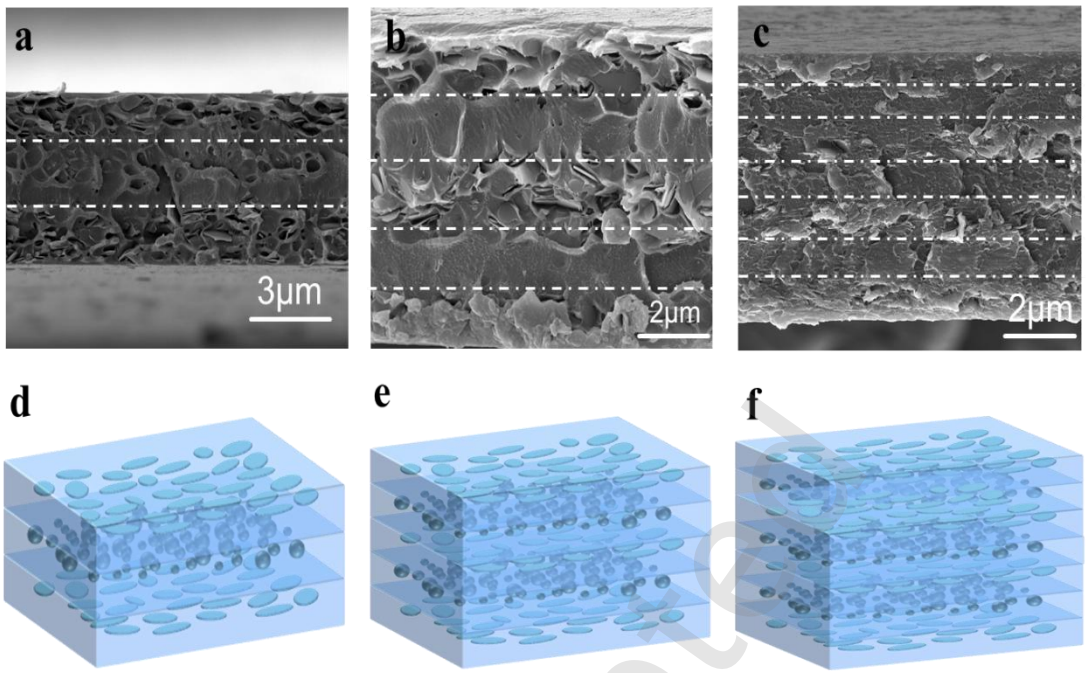

Figure S13. SEM images of (a)3NBN-97,(b) 5NBN-97,(c) 7NBN-97; (d) distribution patterns of 3NBN-97, (e) 5NBN-97, and (f) 7NBN-97.

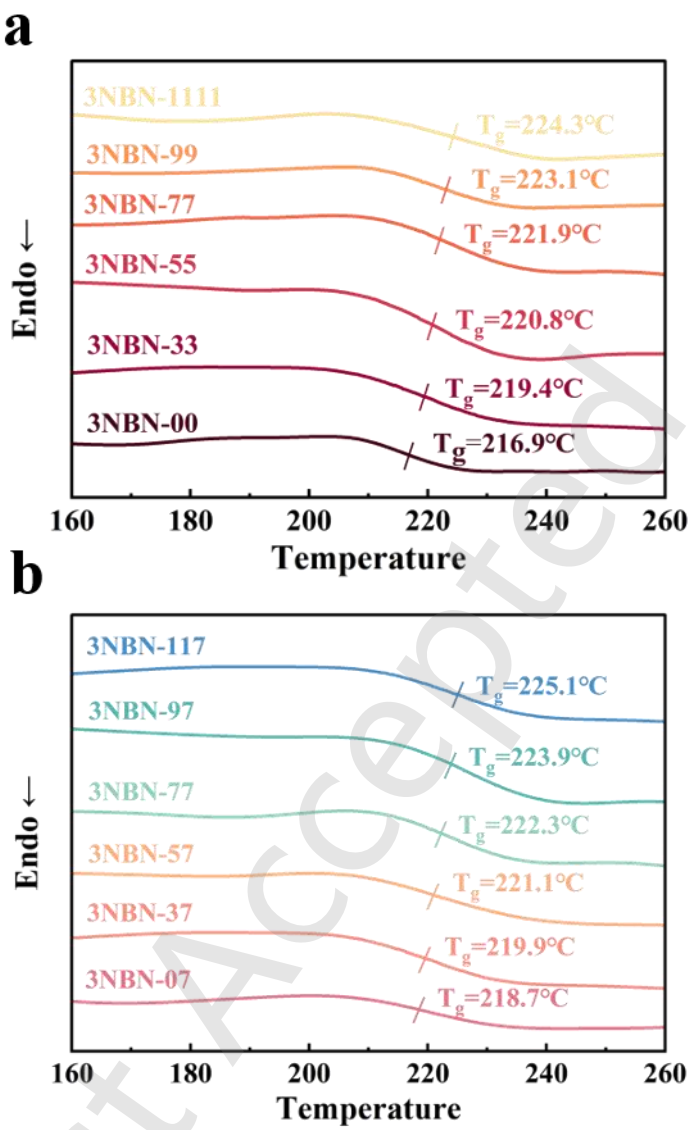

Figure S14. (a, b) DSC curves of 3NBN-xx,3NBN-x7 and xNBN-97.

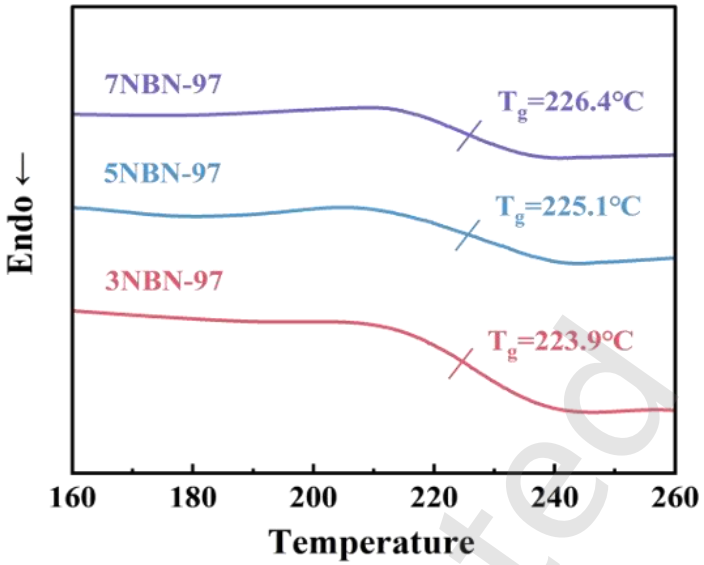

Figure S15. DSC curves of xNBN-97.

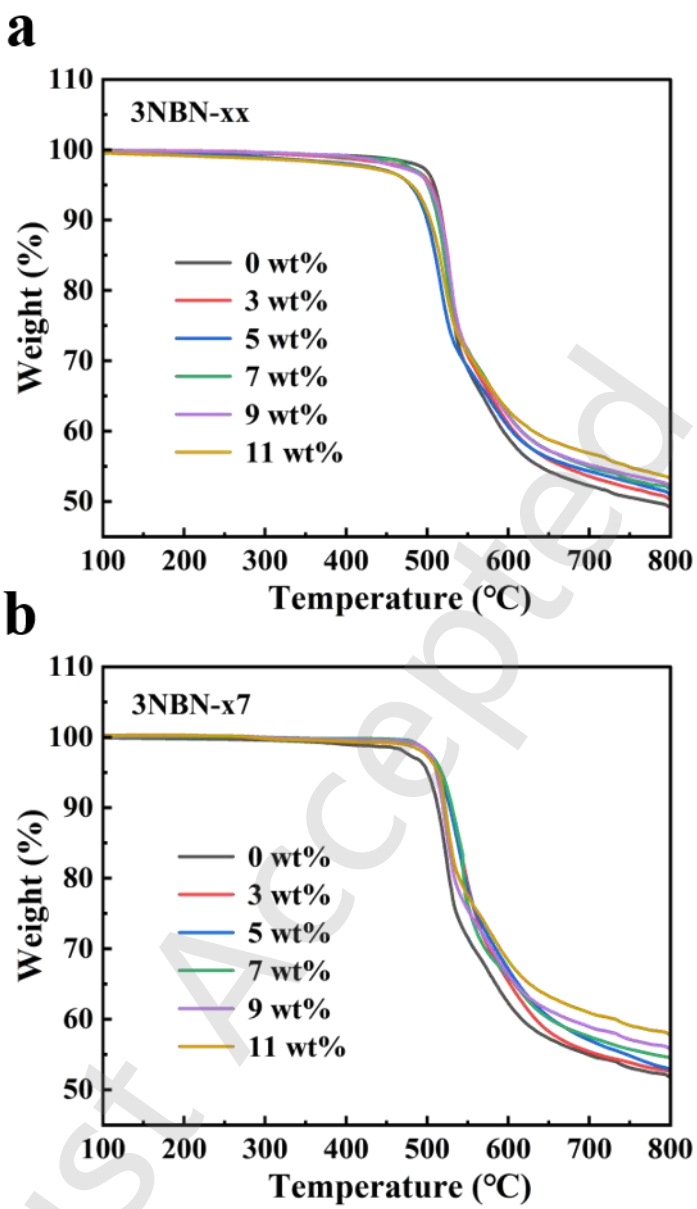

Figure S16. (a, b) TGA curves of 3NBN-xx, 3NBN-x7.

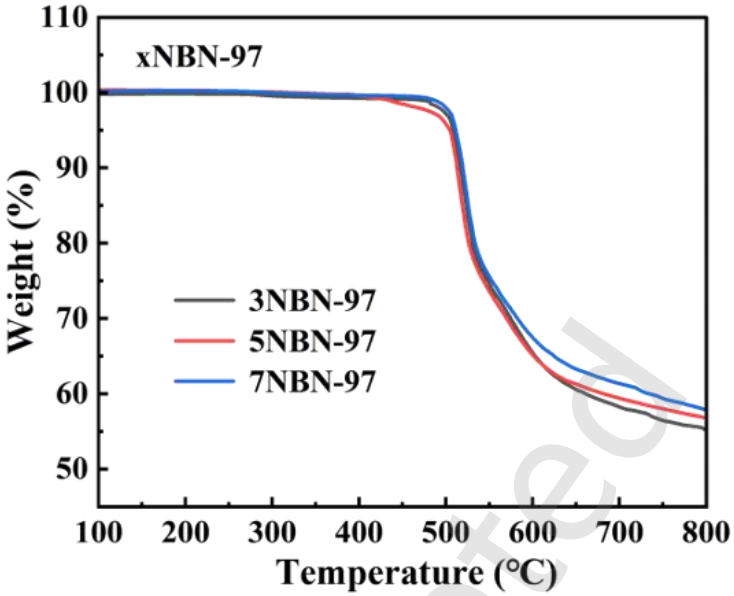

Figure S17. TGA curves of xNBN-97.

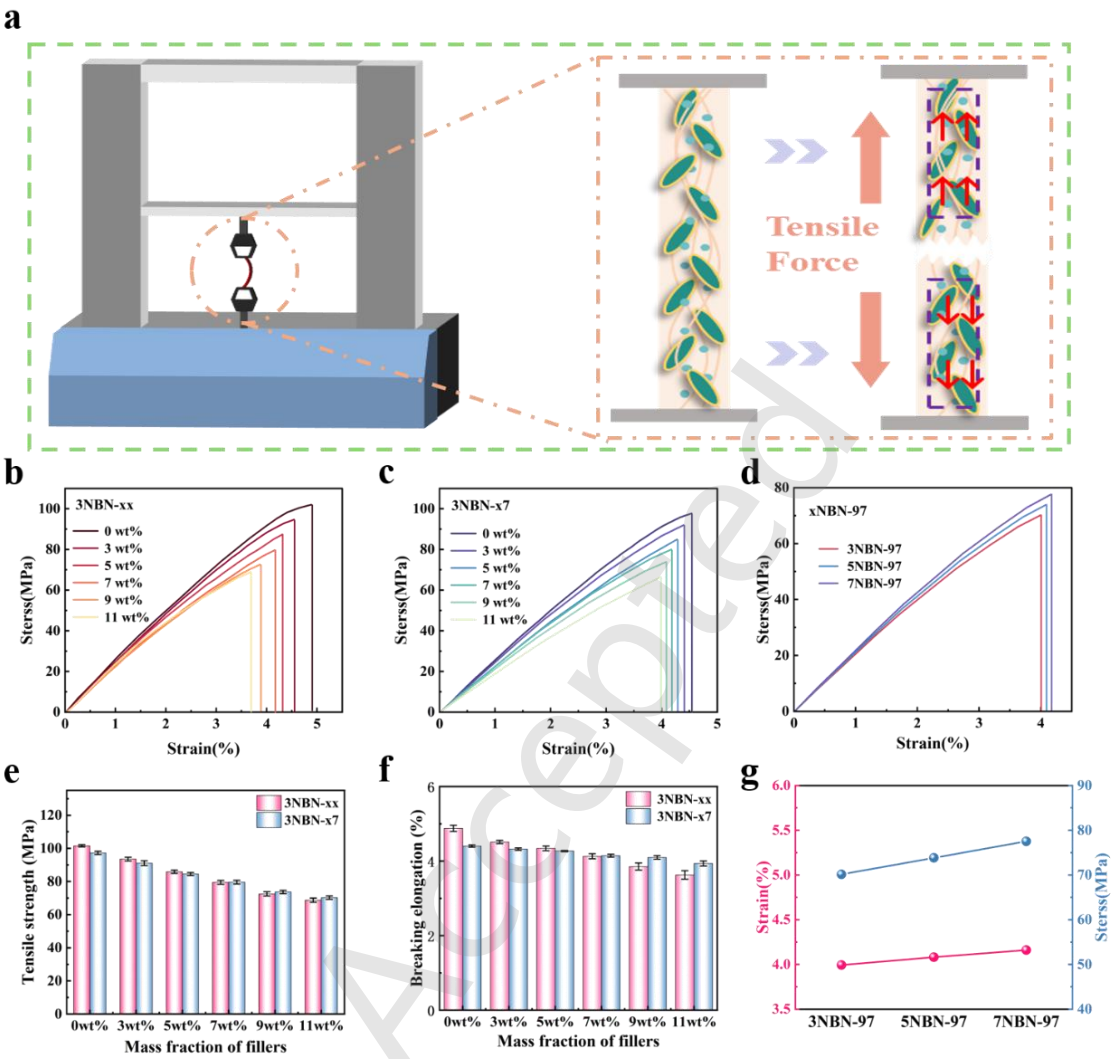

Figure S18. (a) schematic diagram of load transfer during mechanical tests;Stress-strain curves of 3NBN-xx (b), 3NBN-x7 (c) and xNBN-97 (d,g); comparison of tensile strength and elongation at break of 3NBN-xx (e) and 3NBN-x7 (f).

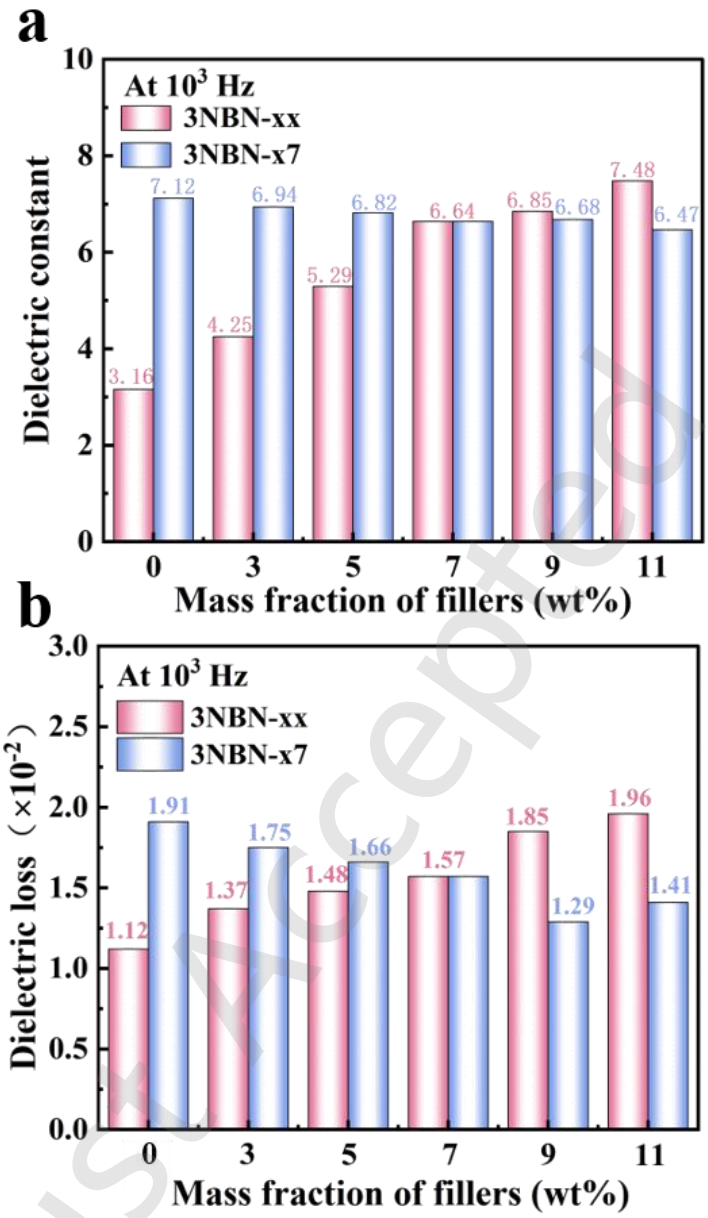

Figure S19. Dielectric constant (a) and dielectric loss (b) of the composites at 1 kHz;

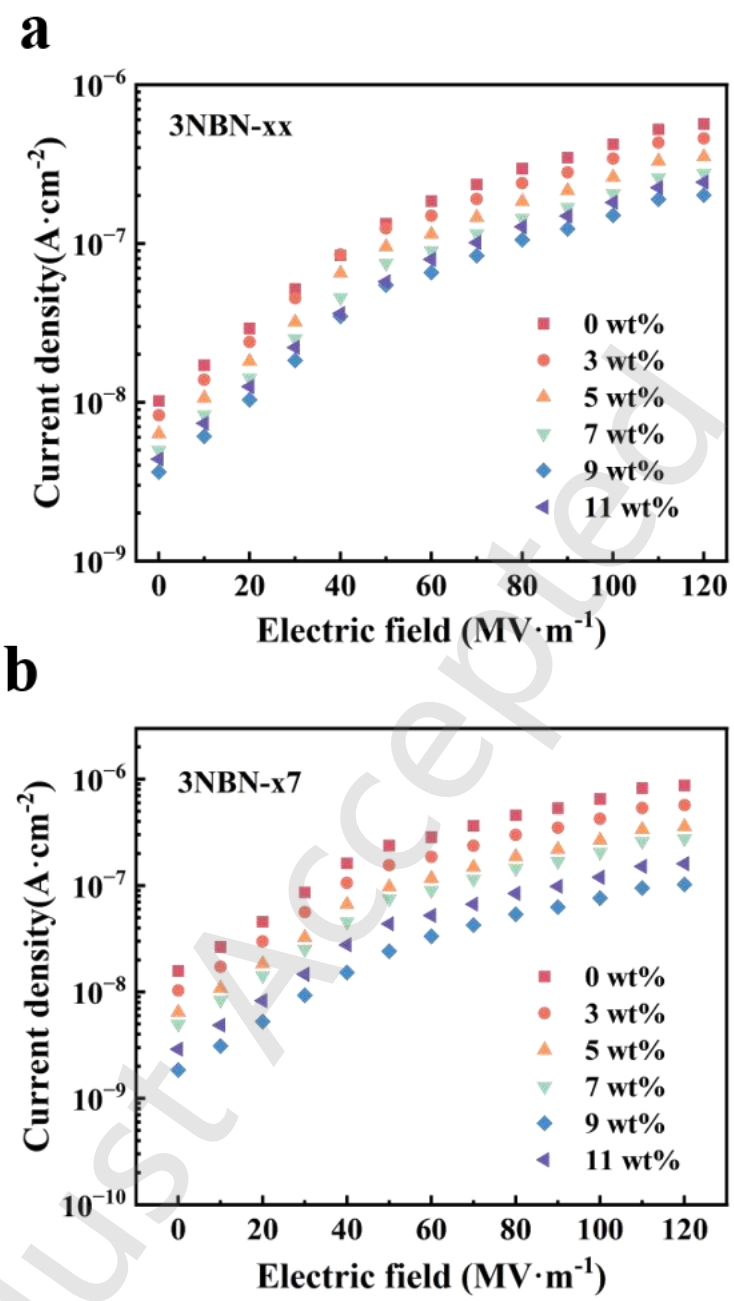

Figure S20. (a, b) Leakage current densities of 3NBN-xx, 3NBN-x7.

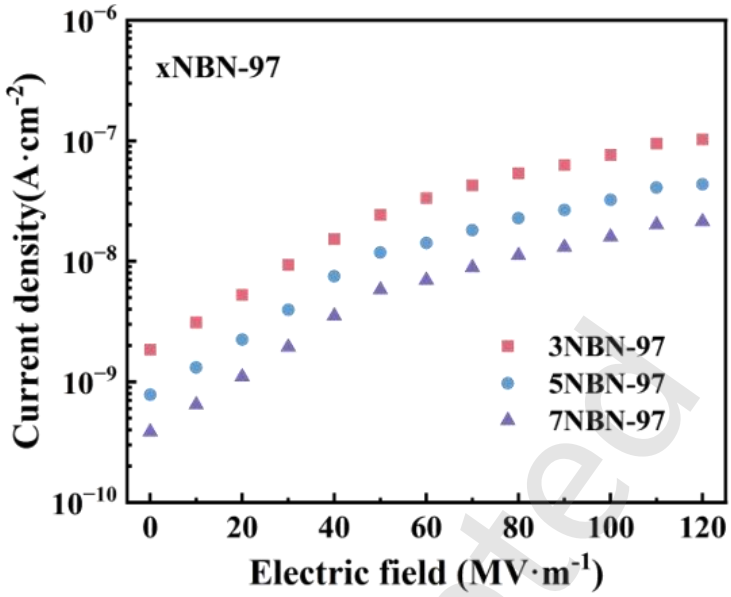

Figure S21. Leakage current density of xNBN-97.

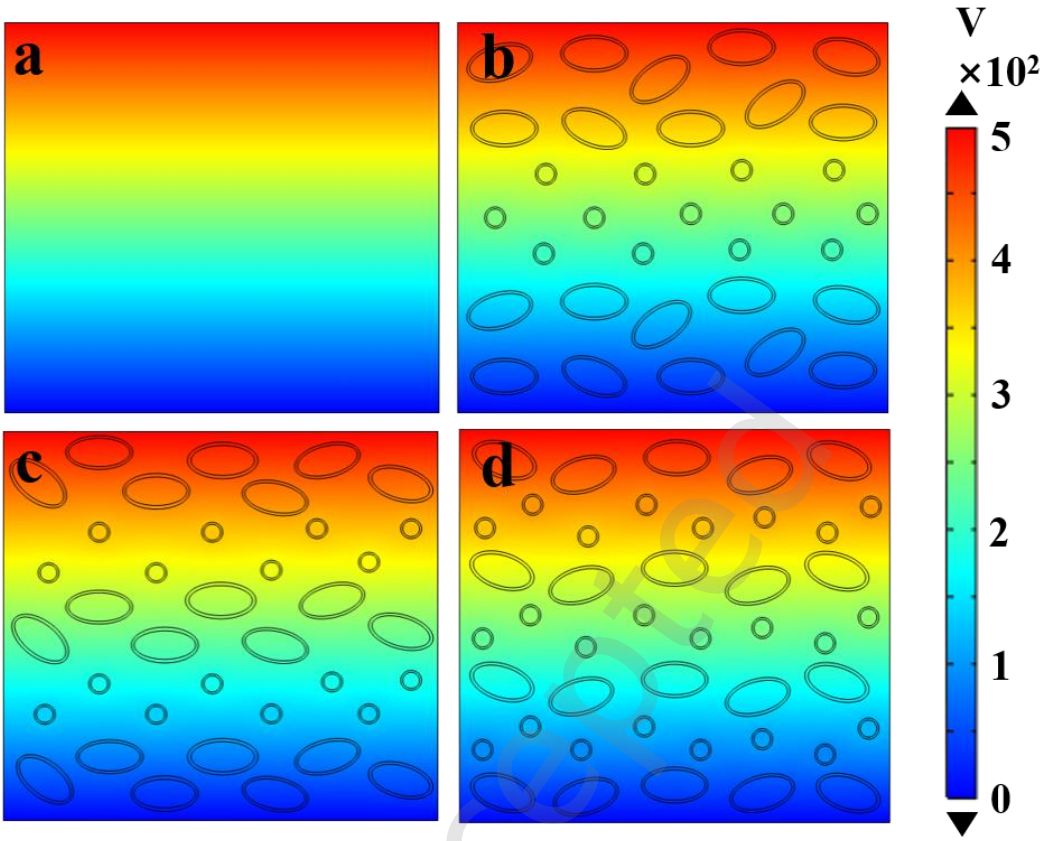

Figure S22. (a–d) Electric potential distribution of pure PEI, 3NBN-97, 5NBN-97 and 7NBN-97.

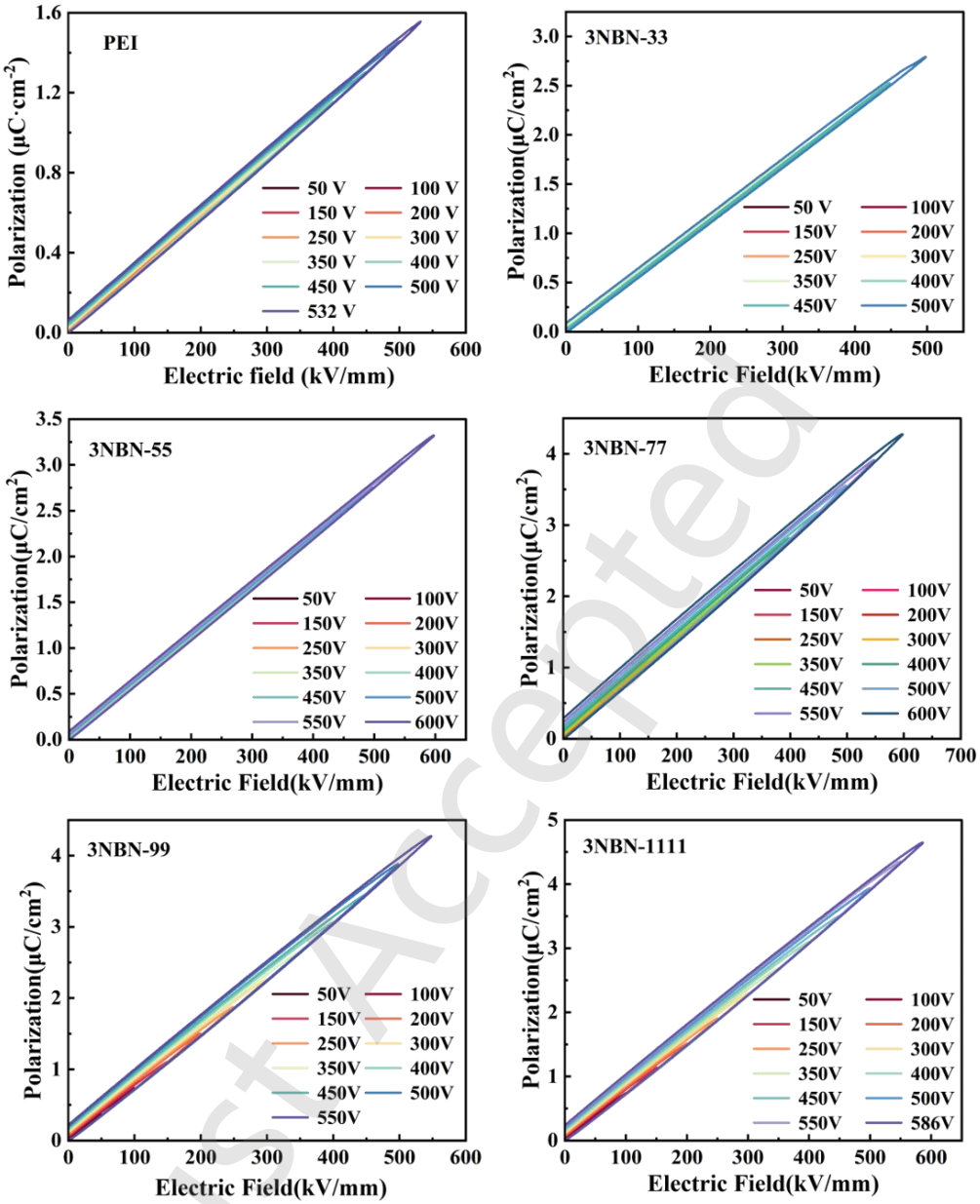

Figure S23. P–E loops before breakdown for 3NBN-xx.

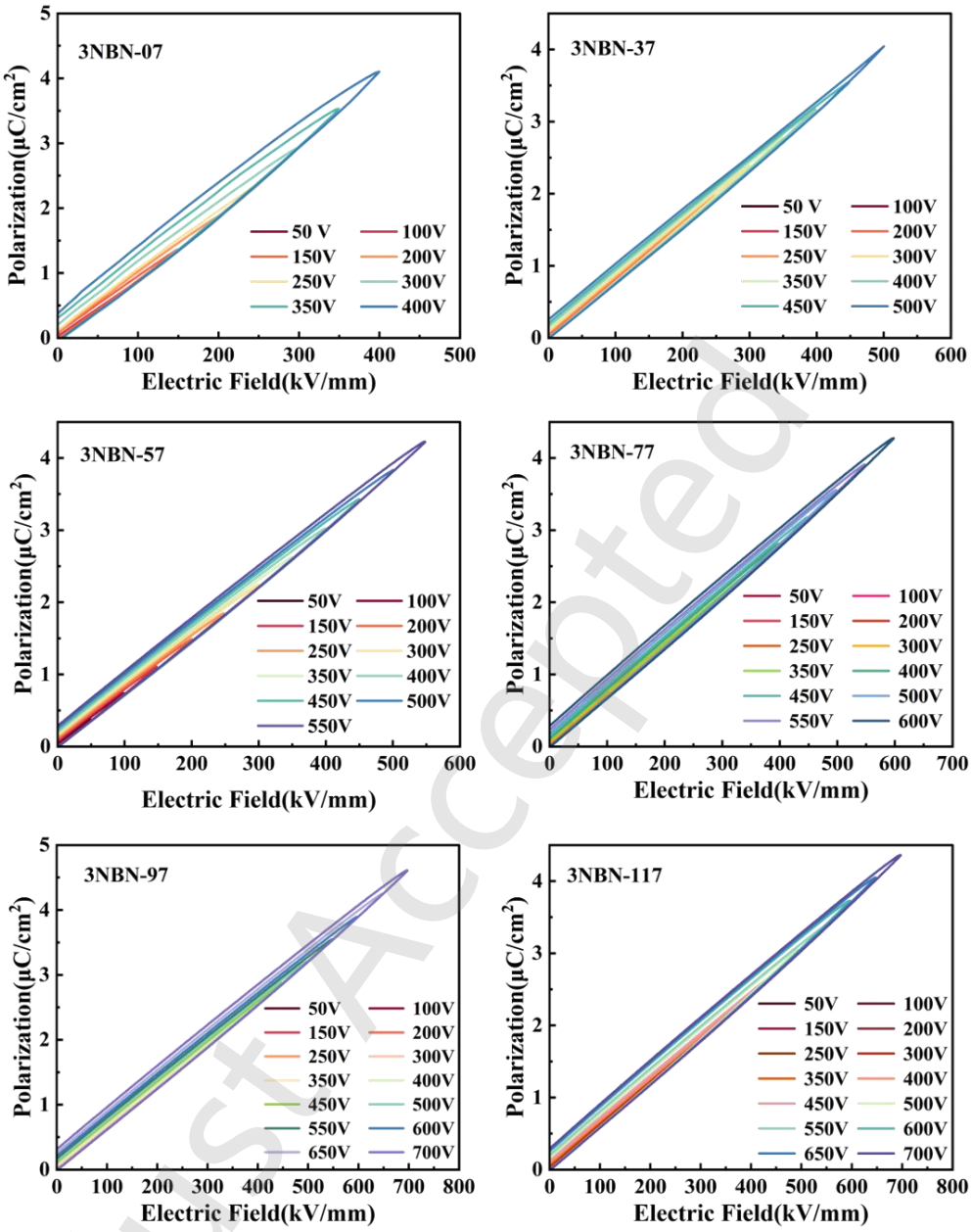

Figure S24. P–E loops before breakdown for 3NBN-x7.

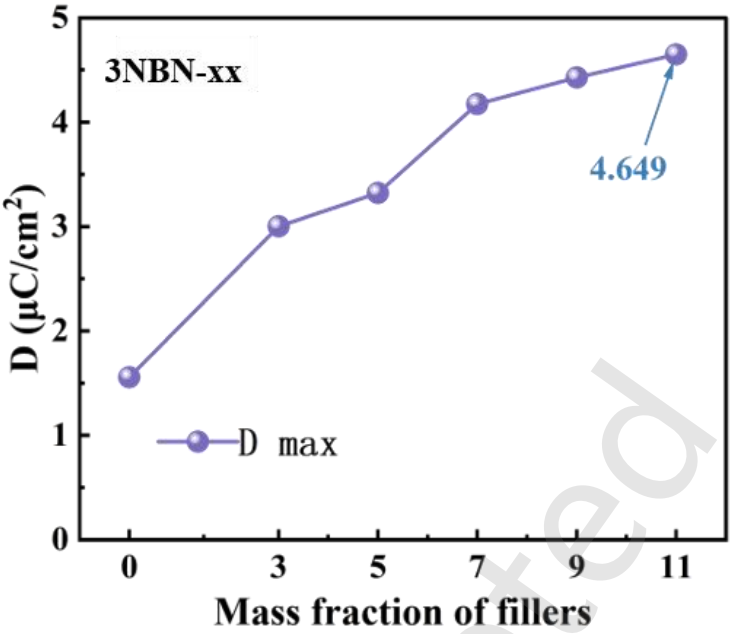

Figure S25. D_{max} of 3NBN-xx.

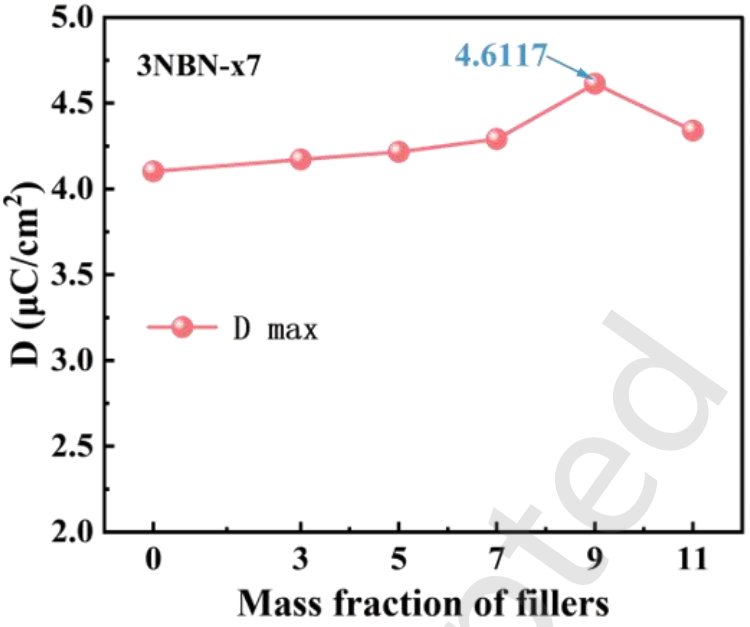

Figure S26. D_{max} of 3NBN-x7

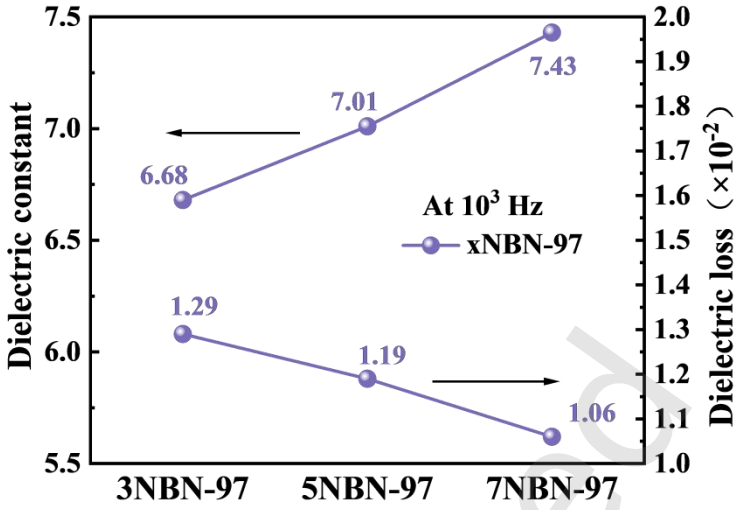

Figure S27. Dielectric constants and dielectric loss of xNBN-97 at 1 kHz .

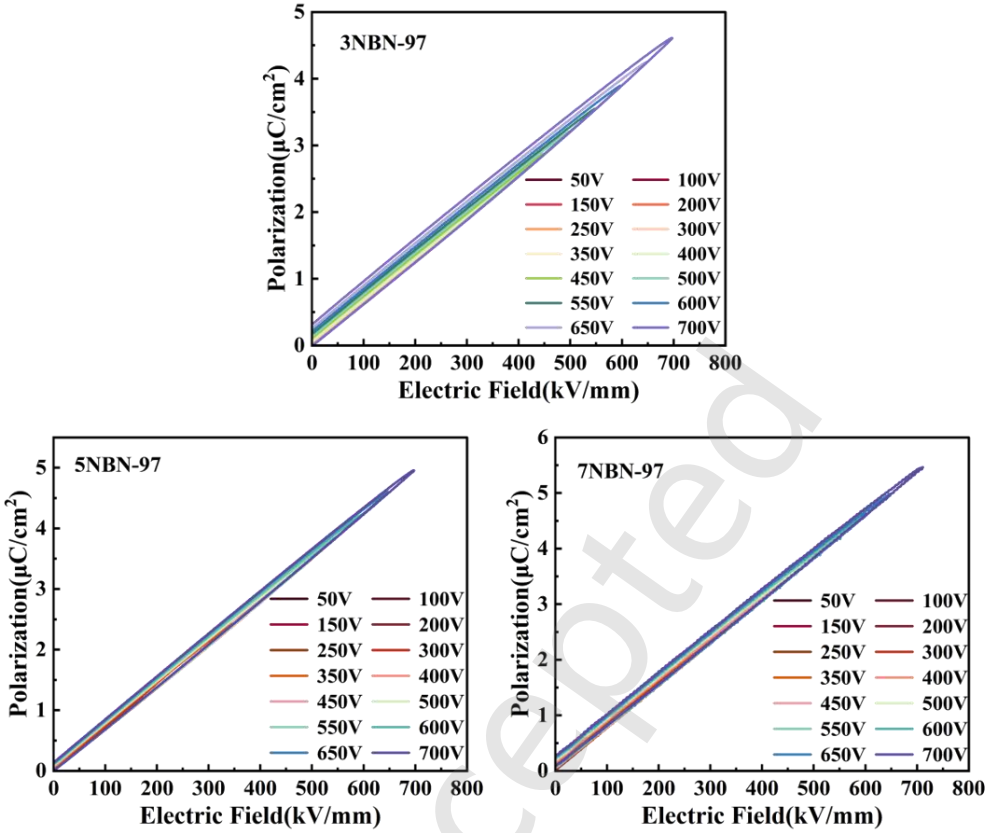

Figure S28. P–E loops before breakdown for xNBN-97.

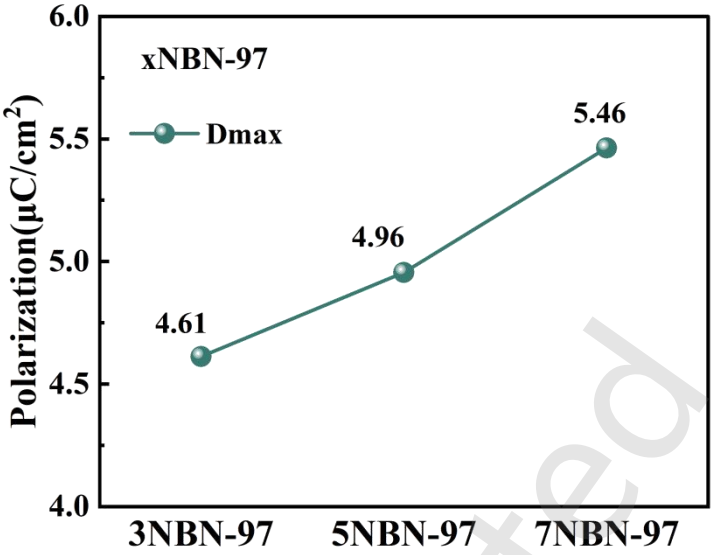

Figure S29. D_{max} of xNBN-97.

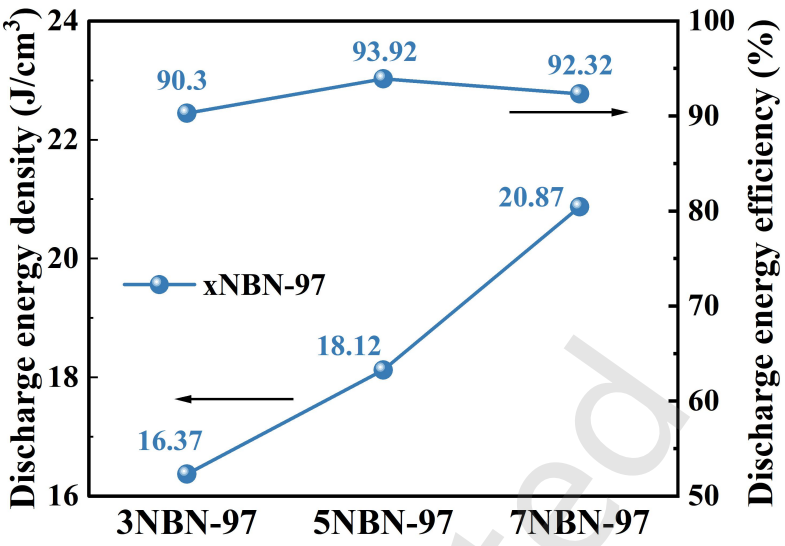

Figure 30. The energy density of xNBN-97.

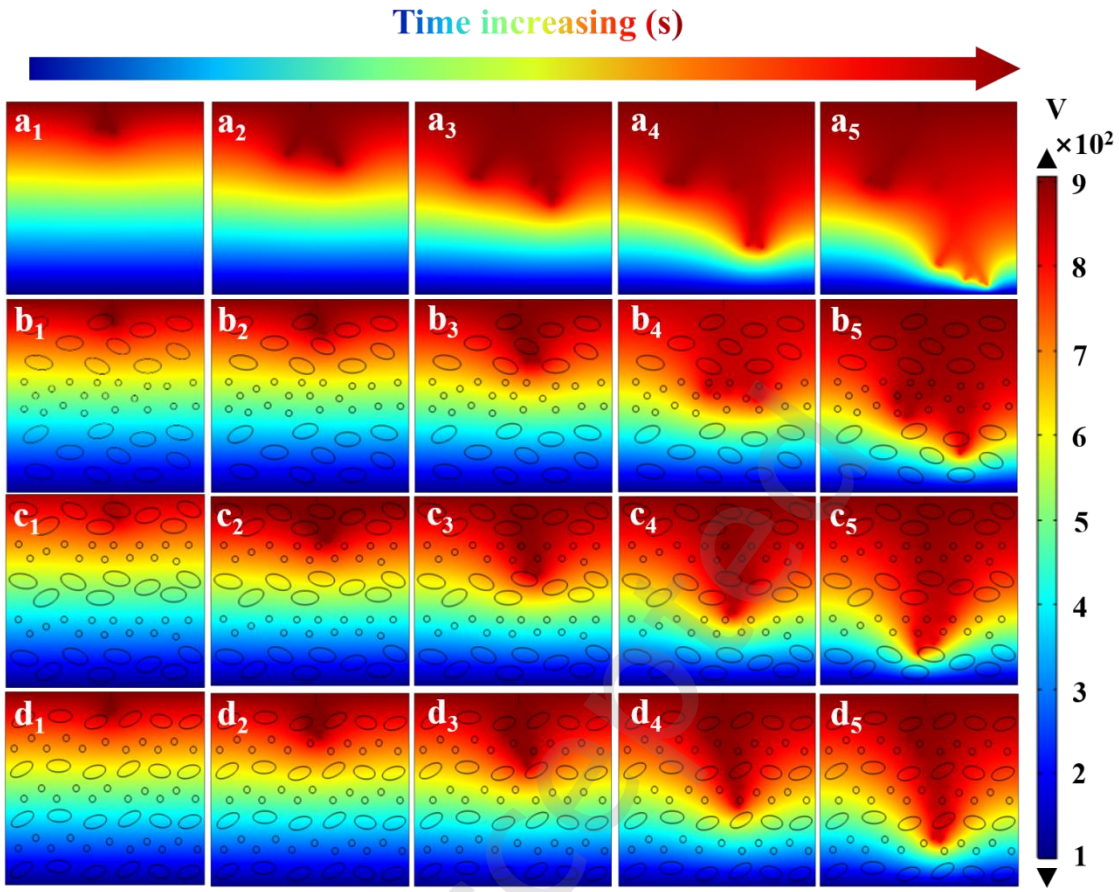

Figure S31. (a_1–a_5) Potential changes during the electrical tree evolution of PEI. (b_1–b_5) Potential changes during the electrical tree evolution of 3NBN-97. (c_1–c_5) Potential changes during the electrical tree evolution of 5NBN-97. (d_1–d_5) Potential changes during the electrical tree evolution of 7NBN-97.

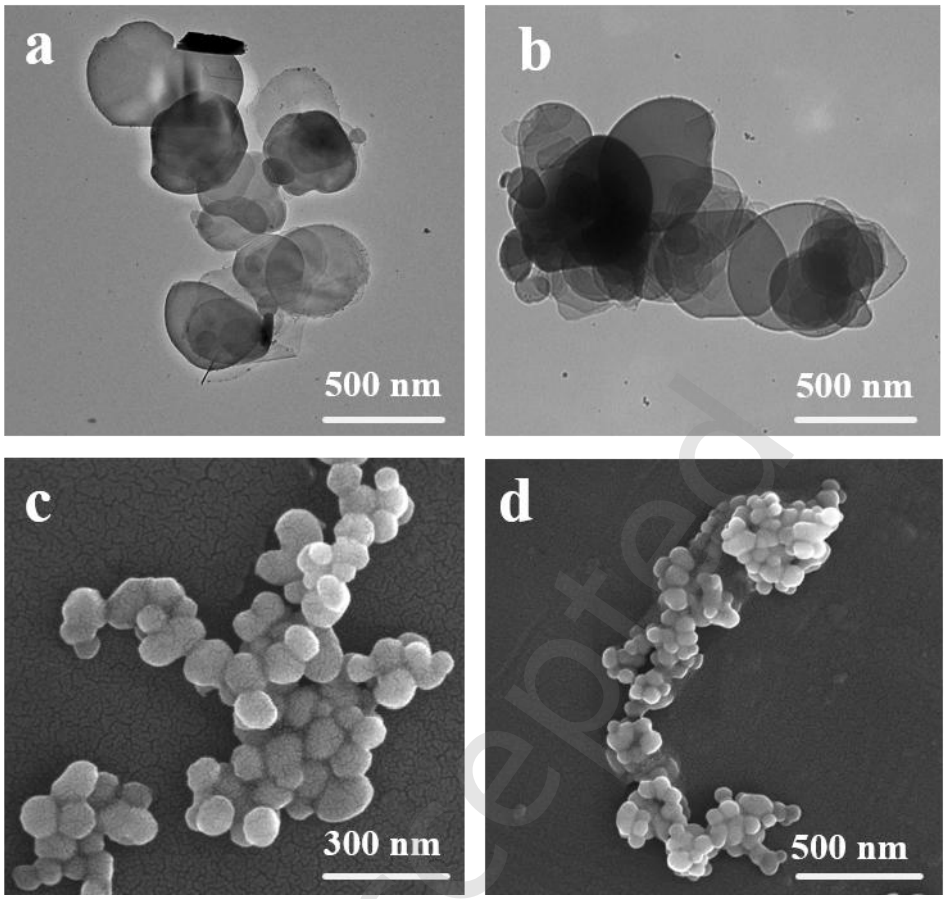

Figure S32 TEM images of (a) CPEI@BNNS and (b) BNNS-KH550; SEM images of (c) CPEI@BST and (d) BST-KH550.

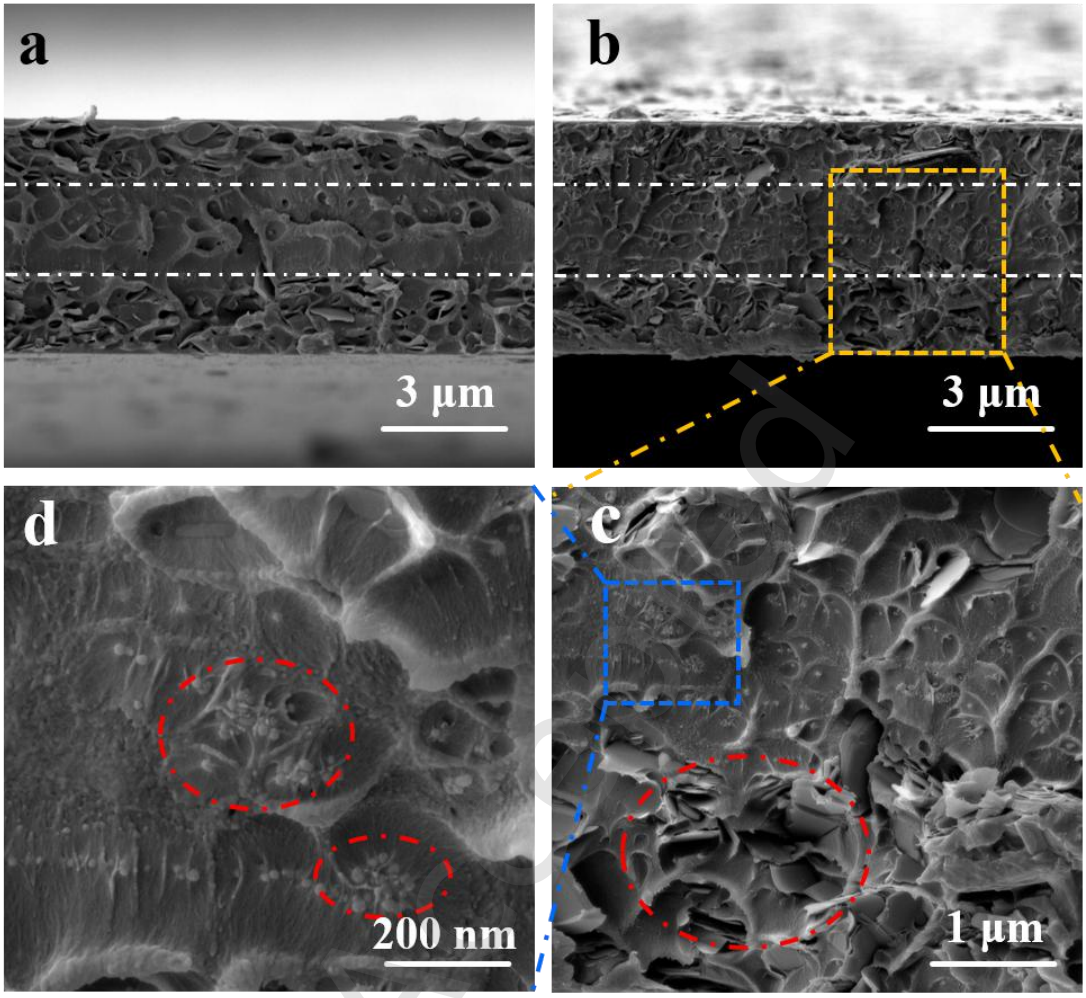

Figure S33 SEM images of (a) 3NBN-97-CPEI and (b-d)3NBN-97-KH550.

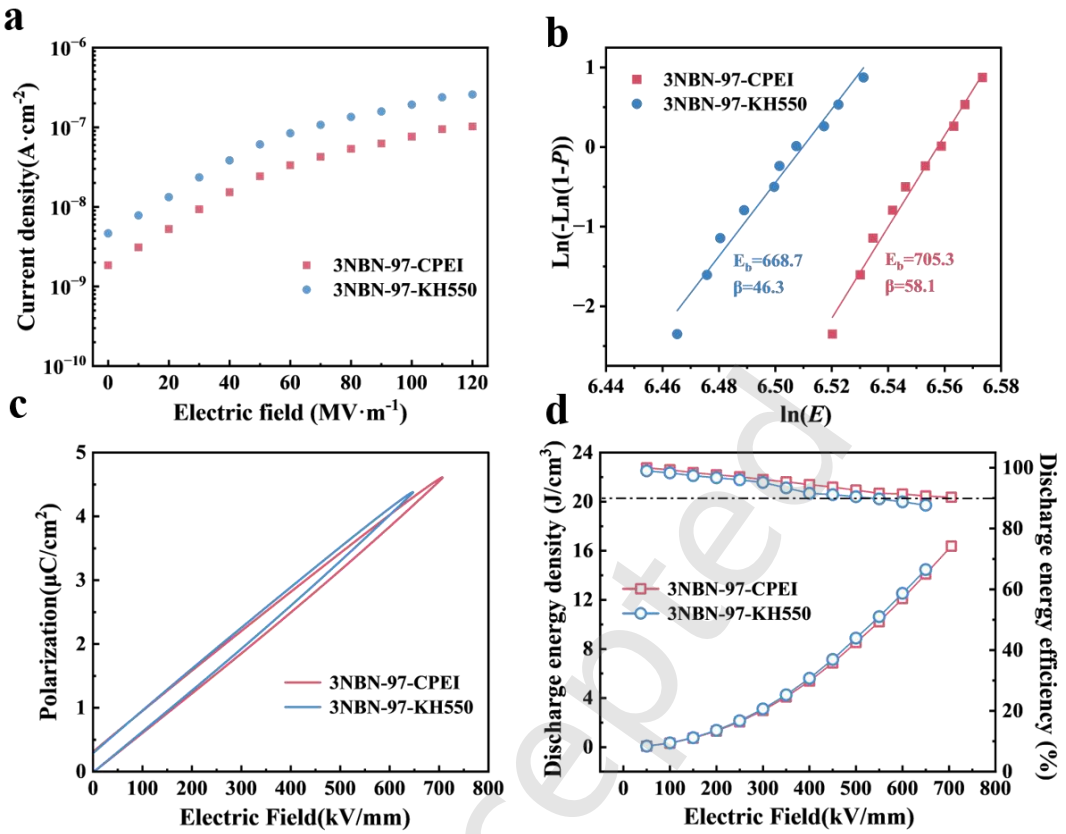

Figure S34 (a) Leakage current density; (b) breakdown strength; (c) P-E loops; and (d) U_d and η of the two modified composites.

Table S1. Summary of h-BN, BNNS-OH, CPEI@BNNS, BST, BST-NH2, CPEI@BST, CPEI, 3NBN-xx, 3NBN-x7 and xNBN-97 residual rate.

Sample	Residual rate (%)
h-BN	98.5
BNNS-OH	96.9
CPEI@BNNS	88.8
BST	98.4
BST-NH2	95.3
CPEI@BST	86.7
CPEI	49.13
Pure PEI	49.28
3NBN-xx (x=3 wt%)	50.35
3NBN-xx (x=5 wt%)	51.19
3NBN-xx (x=7 wt%)	52.48
3NBN-xx (x=9 wt%)	53.34
3NBN-xx (x=11 wt%)	54.28
3NBN-x7 (x=0wt%)	51.07
3NBN-x7 (x=3 wt%)	51.93
3NBN-x7 (x=5 wt%)	52.36
3NBN-x7 (x=9 wt%)	53.27
3NBN-x7 (x=11 wt%)	54.37
5NBN-97	54.84
7NBN-97	56.12

Table S2. Summary of 3NBN-xx, 3NBN-x7 and xNBN-97 dielectrical property.

Sample	εr	tan δ ($\times 10^{-2}$)	E_b (kV/mm)	U_e (J/cm^3)	U_d (J/cm^3)	η(%)
Pure PEI	3.16	1.12	521.1	4.41	4.25	96.3
3NBN-xx (x=3 wt%)	4.25	1.37	535.4	7.62	7.24	94.96
3NBN-xx (x=5 wt%)	5.29	1.48	610	10.85	10.27	94.64
3NBN-xx (x=7 wt%)	6.64	1.57	639.1	15.34	13.87	90.4
3NBN-xx (x=9 wt%)	6.85	1.85	567.9	14.4	12.82	89.1
3NBN-xx (x=11 wt%)	7.48	1.96	584.1	15.57	13.8	88.6
3NBN-x7 (x=0wt%)	7.12	1.91	413.6	9.19	7.88	85.76
3NBN-x7 (x=3 wt%)	6.94	1.75	511.8	11.2	10.27	91.67
3NBN-x7 (x=5 wt%)	6.82	1.66	568.1	13.27	11.94	90
3NBN-x7 (x=9 wt%)	6.68	1.29	705.3	18.13	16.37	90.3
3NBN-x7 (x=11 wt%)	6.47	1.41	724.8	18.01	15.78	87.6
5NBN-97	7.01	1.19	716.2	19.29	18.12	93.92
7NBN-97	7.43	1.06	731.2	22.6	20.87	92.32

References

[1] Klein, J.; Kampermann, L.; Mockenhaupt, B.; Behrens, M.; Strunk, J.; Bacher, G. Limitations of the Tauc Plot Method. Adv. Funct. Mater. 2023, 33, 2304523.

[2] Zeng, F.; Ji, C.; Xiang, Z.; Gao, L.; Xu, W.; Peng, Z. Optical band gap determination of carbon dots: A critical comparison of tangent and Tauc plot methods benchmarked with metal oxides. Carbon 2026, 249, 121239.

[3] Mıhçıokur, Ö.; Özpozan, T. Molecular structure, vibrational spectroscopic analysis (IR & Raman), HOMO-LUMO and NBO analysis of anti-cancer drug sunitinib using DFT method. J. Mol. Struct. 2017, 1149, 27-41.

[4] Wei, R.; Jiao, Y.; Liu, Y.; Wang, Z.; Zhao, X.; Bao, S.; Wang, L.; Dang, Z. M.; Zheng, X.; Hua, X. Hot stretching induced Orientation of Calcium Copper Titanate Nanorods in Polyetherimide for Enhanced Energy Storage Density. Small 2025, 22, e13033.

[5] Cai, Z.; Wang, X.; Li, L.; Hong, W. Electrical treeing: A phase-field model. Extreme Mech. Lett. 2019, 28, 87-95.

[6] Wang, Z.; Feng, Z.; Tang, H.; Wang, J.; Cai, Z.; Bi, K.; Hao, Y. Effects of Nanofibers Orientation and Aspect Ratio on Dielectric Properties of Nanocomposites: A Phase-Field Simulation. ACS Appl. Mater. Interfaces 2022, 14, 42513-42521.